Applied Catalysis B: Environmental 324 (2023) 122240

Contents lists available at ScienceDirect

Applied Catalysis B: Environmental

journal homepage: www.elsevier.com/locate/apcatb

Reduced anodic energy depletion in electrolysis by urea and water co-oxidization on NiFe-LDH: Activity origin and plasma functionalized strategy

Dan Li [a], Xiaomin Zhou [a], Liangliang Liu [a], Qingdong Ruan [a], Xiaolin Zhang [a], Bin Wang [a], Fangyu Xiong [a], Chao Huang [a,b,*], Paul K. Chu [a,**]

[a] Department of Physics, Department of Materials Science and Engineering, and Department of Biomedical Engineering, City University of Hong Kong, Tat Chee Avenue, Kowloon, the Hong Kong Special Administrative Region of China
[b] State Key Laboratory of Powder Metallurgy, Central South University, Changsha 410083, China

ARTICLE INFO

Keywords:
Urea oxidization reaction
NiFe-layered double hydroxide
Active sites
Plasma processing
Energy saving

ABSTRACT

As an alternative anodic reaction to water oxidization (oxygen evolution reaction, OER), the urea oxidization reaction (UOR) is promising due to its favorable thermodynamics. However, reliance of the proper Ni oxidization state and passivation at high potentials render UOR by Ni-based catalysts inefficient and impractical. Herein, the anodic characteristics of the conventional NiFe-layered double hydroxide (NiFe-LDH) catalyst are investigated in a urea-containing alkaline electrolyte. Fe^{3+} and derivative $Ni^{2+\delta}$ cations are identified as the UOR active sites before and after Ni oxidization and both UOR and OER are observed simultaneously at high potentials. The number of active sites increases at high potentials and internal atoms are activated as well. For further improvement, plasma processing is employed to produce layer reconstruction on the NiFe-LDH slabs in a controllable fashion, leading to left-shifting of the Ni oxidization threshold and enhanced UOR activity. The assembled urea-assisted hydrogen evolution device is demonstrated to have better energy-saving and passivation-avoiding characteristics.

1. Introduction

In order to reduce the environmental impact, electrocatalysis is the ideal strategy for hydrogen generation, carbon dioxide reduction, and contaminants degradation [1–5]. However, in conventional water oxidization using electrolytic devices, the oxygen evolution reaction (OER) occurring on the anode consumes most of the electrical power. For example, 92.2% of the energy is consumed by OER in reduction of carbon dioxide to form carbon oxide according to the thermodynamic calculation [6]. In recent years, urea [7–9], hydrazine [10–12], and biomass [6,13–16] oxidization has been proposed as alternative anodic reactions [17]. Among them, the urea oxidization reaction (UOR) is meaningful in mitigating environmental problems such as sewage disposal leading to excessive urea release (high-valance nitrogen compounds) [8]. Nonetheless, owing to the multiple electron transfer process in these reactions, the reaction kinetics is sluggish and must be improved.

UOR with a favorable thermodynamic potential (0.37 V) is a promising alternative anodic reaction that consumes about 70% less energy than OER in theory [18]. However, most electrocatalysts with limited functional sites cannot overcome the six-electron transfer energy barrier resulting in unsatisfactory overpotentials. For example, although advanced Ni-based catalysts are effective because the UOR potential is lower than that in OER, most onset potentials in UOR are around 1.3 V vs. RHE, as summarized by You et al. [17] The problem stems from the reliance of the oxidation state of Ni-based materials. The derived high valance states of Ni cations at the anodic potentials are identified to be active and the reaction is more likely to proceed through the chemical pathway. However, it has recently been shown that the $NiFe(CN)_6$ catalyst can catalyze UOR with low-valance Ni cations [9] thus complicating the origin of the activity of the Ni-based materials.

In evaluating the effectiveness of catalysts, the high potential

* Corresponding author at: Department of Physics, Department of Materials Science and Engineering, and Department of Biomedical Engineering, City University of Hong Kong, Tat Chee Avenue, Kowloon, the Hong Kong Special Administrative Region of China.
** Corresponding author.
E-mail addresses: chuang46-c@my.cityu.edu.hk (C. Huang), paul.chu@cityu.edu.hk (P.K. Chu).

https://doi.org/10.1016/j.apcatb.2022.122240
Received 14 October 2022; Received in revised form 16 November 2022; Accepted 28 November 2022
Available online 30 November 2022

operation in addition to onset potential must be taken into consideration. A typical example is $Ni(OH)_2$, which shows an impressive onset potential, but exhibits a peak current (passivation) at high potentials as revealed by cyclic voltammetry (CV) [19,20]. The competing OER may be responsible for passivation in UOR since accumulation of OER intermediates at high potentials poisons the active sites and consequently reduces the currents [7]. Designing a catalyst with intrinsic thermodynamic superiority is an effective strategy to avoid passivation, but since the UOR activity depends on the oxidation state of the electrocatalyst, reduction of the onset potentials alone may not be the best strategy. On the other hand, from the perspective of mitigating energy consumption in electrocatalytic hydrogen generation or carbon dioxide reduction, performing OER and UOR in concert in the high potential region may offer a better solution. One of the promising electrocatalysts is the NiFe-layer double hydroxide (NiFe-LDH), which shows favorable thermodynamics in OER and superior oxidizing ability after phase reconstruction at high potentials [21,22]. However, there have been few reports about UOR at high potentials. Moreover, although NiFe-LDH is effective in UOR in terms of the onset potential [23,24], the activity origin or mechanism is not well understood due to the changes of the materials during the process.

Herein, using thin NiFe-LDH nanosheets self-anchored on the Ni foam as an example, the dynamic active sites during UOR at various potentials are investigated systematically by *operando*, *quasi-operando*, and time-varying methods in addition to steady-state measurements and transient electrochemical techniques. Argon (Ar) plasma processing is further employed to produce restacking of the NiFe-LDH nanosheets to improve the UOR characteristics and elucidate the activity origin. Finally, the feasibility and advantages of the urea-assisted electrocatalytic hydrogen generation system such as energy-saving are demonstrated using NiFe-LDH as the anode.

2. Experimental methods

2.1. Materials and chemicals

$Ni(NO_3)_2{\cdot}6\ H_2O$ (~99.9%), $Fe(NO_3)_3{\cdot}9\ H_2O$ (~98.5%), urea (~99.0%), and KOH (~ 90.0%) were purchased from Sigma Aldrich. The Ni foam (thickness: 1.6 mm; bulk density: 0.45 g cm^{-3}) was purchased from Goodfellow. All the chemicals used were analytical grade and deionized water was used throughout the experiments.

2.2. Synthesis of NiFe-LDH nanosheets on Ni foam

The NiFe NiFe-LDH nanosheets were self-anchored on the Ni foam (2 cm × 4 cm) by a hydrothermal method. The bare Ni foam was sonicated in 20% HCl, acetone, and deionized water for 15 mins sequentially and then 0.75 mmol $Ni(NO_3)_2{\cdot}6\ H_2O$, 0.25 mmol $Fe(NO_3)_3{\cdot}9\ H_2O$, and 6 mmol urea were dissolved in 45 mL of deionized water to form a homogeneous solution by vigorous stirring. Afterwards, the Ni foam was immersed in the solution, transferred to a 50-mL Teflon-lined autoclave, sealed, and maintained at 120 °C for 10 h. After cooling to room temperature naturally, the sample was removed, rinsed with ethanol and deionized water successively, and dried at 40 °C for 6 h in air.

2.3. Plasma processing of NiFe-LDH

The dry NiFe-LDH on the Ni foam was transferred to a high vacuum capacitively-coupled plasma (CCP) reactor and processed in an Ar plasma. The discharge power was 40 W, pressure was 20 mT, and Ar flow rate was 20 sccm. The NiFe-LDH-0, NiFe-LDH-20, NiFe-LDH-40, NiFe-LDH-60 samples to be used as NiFe-LDH electrodes were plasma treated for 0, 20, 40, and 60 min, respectively.

2.4. Synthesis of $Ni(OH)_2$ and plasma-processed Ni foam electrodes

The $Ni(OH)_2$ electrode was synthesized hydrothermally as described in Ref. 7. The Ni foam was transferred to the high vacuum CCP reactor and etched by the Ar plasmas for 30 min using a discharge power of 20 W, pressure of 20 mT, and Ar flow rate of 20 sccm.

2.5. Materials characterization

The XRD patterns were obtained on the Rigaku Smartlab X-ray diffractometer. Sample alignment was performed before the test and in the *quasi-operando* measurement, XRD was carried out within 5 min after the electrochemical measurement. The scanning rates in the small-angle and full tests were 0.5° min^{-1} and 10 min^{-1}, respectively. SEM was performed on the Thermo scientific Quattro S and TEM was conducted on the FEI Tecnai G2 F20. The XPS spectra were acquired on the Thermo scientific Escalab 250Xi. The C 1 *s* peak at 284.6 eV was used to calibrate the XPS spectra. Raman scattering was carried out on the HORIBA Scientific Lab RAM HR Raman spectrometer using the 514.5 nm green laser excitation and in the *operando* Raman experiments, the spectra were acquired under the specific electrochemical conditions (given voltages in the Amperometric i-t technique).

2.6. Electrochemical assessment

CV, LSV, EIS, i-t amperometry, and OCP-time measurements were conducted on the CHI 660E potentiostat equipped with a typical three-electrode system, in which the Hg/HgO electrode (filled with 1 M KOH) and graphite were the reference and counter electrodes, respectively. The Pt wire counter electrode was used in the *operando* Raman scattering test. The OER and UOR electrolytes were 1 M KOH and 1 M KOH with 0.5 M urea, respectively. The distance between the working electrode and counter electrode was approximately 1.5 cm and all the measurements were conducted at room temperature. The CV and LSV curves were obtained at a scanning rate of 5 mV s^{-1} except the activation process (10 mV s^{-1}). To be practical and reflect the operating conditions in the high potential region, the potentials were not iR corrected unless otherwise stated. The UOR potentials were derived from the forward sweep, whereas the OER potentials were the values in the backward sweep. The current densities were recorded based on the geometric area unless otherwise stated (mA cm^{-2}). EIS was performed with an alternating current voltage amplitude of 5 mV and the stability was evaluated according to successive amperometry i-t curves and chronopotentiometry.

3. Results and discussion

3.1. UOR on NiFe-LDH

The NiFe-LDH nanosheets (200–500 nm in size and ~10 nm thick) are prepared on the Ni foam by a simple hydrothermal method and analyzed using a three-electrode system as mentioned above. Fig. 1a shows the cyclic voltammetry (CV) curves of the NiFe-LDH electrode in the urea-containing and urea-free electrolytes showing that UOR occurs before OER. Analysis of the kinetics reveals that the onset potential in UOR is independent of the urea concentration after addition of 0.1 M urea and the current densities at high potentials are stable when the urea concentration reaches 0.5 M (Fig. S1). Therefore, 0.5 M urea is used in our subsequent experiments and analysis. Because of the fast UOR or OER response, the oxidization peak of Ni ($Ni(OH)_2/Ni^{2+\delta}O_xH_y$) is covered. In the UOR curve, the electro-reduction peak of the derivative $Ni^{2+\delta}O_xH_y$ (NiOOH and NiO_x) is suppressed and the backward sweep current is larger than that in the forward one, suggesting that $Ni^{2+\delta}O_xH_y$ is likely to oxidize urea spontaneously. Because the more robust interaction with –OH of Fe cations (Lewis acid) on NiFe-LDH results in right-shifting of the Ni oxidization peak ($Ni^{2+}/Ni^{2+\delta}$) [25,26], the onset

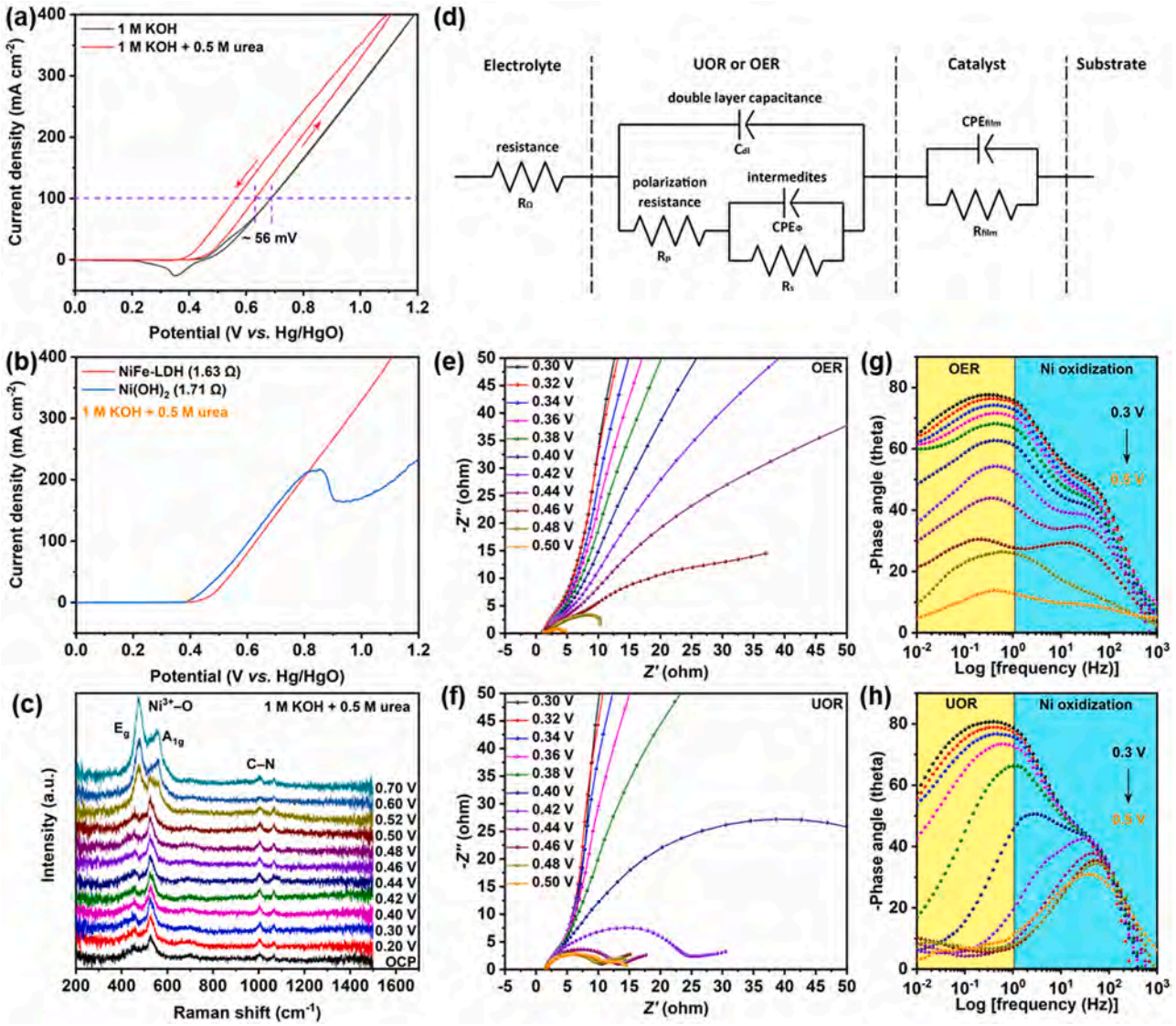

Fig. 1. (a) CV curves of NiFe-LDH in the UOR and OER electrolytes; (b) LSV curves of NiFe-LDH and $Ni(OH)_2$ in the UOR electrolytes; (c) *Operando* Raman scattering spectra of NiFe-LDH in the UOR electrolytes; (d) Equivalent circuit of UOR or OER on the Ni-based hydroxide electrode; *Operando* Nyquist plots and corresponding Bode-phase plots of NiFe-LDH: (e, g) OER electrolyte and (f, h) UOR electrolyte. All the potentials are referenced to the Hg/HgO electrode.

potential of UOR is negative compared to the Ni oxidization threshold (peak overlapping with that in OER). Hence, UOR on the NiFe-LDH electrode can occur on both the pristine NiFe-LDH and derivative $Ni^{2+\delta}O_xH_y$. In the comparative study of the UOR characteristics with the conventional $Ni(OH)_2$ catalyst, NiFe-LDH shows no prominent passivation peak and the current density surpasses that of $Ni(OH)_2$ after 0.81 V, despite the onset potential superiority of $Ni(OH)_2$ (Fig. 1b). Regardless of the origin of the current contribution, the excellent electrochemical characteristics divulge obvious advantages of NiFe-LDH in urea-assisted electrocatalysis, especially in terms of energy-saving.

3.2. Active sites in the low potential region

Operando Raman scattering is carried out to monitor the surface evolution as shown in Fig. S2 and the Raman scattering spectra of NiFe-LDH acquired from the open circuit potential (OCP) to 0.7 V in UOR are displayed in Fig. 1c. Besides the peak at 1004 cm^{-1} assigned to symmetrical C–N stretching of urea molecules [8,27], the two peaks at 455 cm^{-1} and 527 cm^{-1} are attributed to the Ni^{2+}–OH and Fe^{3+}–OOH stretching modes, respectively [25,28,29]. As the potential increases, the initial peak remains stable until 0.50 V and afterwards, the Ni^{3+}–OOH depolarized E_g mode (bending vibration) at 473 cm^{-1} and polarized $A_{1\,g}$ mode (stretching vibration) at 560 cm^{-1} dominate suggesting formation of the γ-NiOOH phase [8,29,30]. Because of the resonance effects as the excitation wavelength approaches the energy of the electronic transition, these two vibrations have larger Raman cross-sections giving rise to larger signal-to-noise ratios [30,31]. It should be noted that our observation of NiFe-LDH is different from that of $Ni(OH)_2$ reported previously. In the case of α-$Ni(OH)_2$, the additional strong Ni^{2+}–O vibration peak at 495 cm^{-1} suggests that the $Ni(OH)_5O^-$ intermediates from dehydrogenation of $Ni(OH)_6$ octahedrons are active in UOR in the low potential region (peak between 0.3 and 0.4 V) [8]. With regard to NiFe-LDH, the peak starts to emerge at 0.50 V (representing formation of $Ni(OH)_5O^-$ intermediates, Fig. S3) and hence, protons and electrons in urea are likely to be sequestered by Fe^{3+} sites below 0.50 V as shown by the persistent Fe^{3+}–OOH vibration signal before γ-NiOOH formation. After the phase transition, the Fe^{3+}–OOH vibration peak disappears perhaps due to transfer of absorbed –OH from Fe to Ni sites and consequently, the formed $Ni^{2+\delta}O_xH_y$ is likely to be the active center in the high potential region.

Electrochemical impedance spectroscopy (EIS) is a useful technique to probe the kinetics of interfacial reactions. Generally, the EIS

responses in the electrocatalytic reactions on self-oxidized catalysts can be characterized by three relaxation processes and the typical circuit model is depicted in Fig. 1d [32]. The three capacitance peaks and pseudo-semicircles are exhibited in the Bode-phase and Nyquist plots, respectively [19,33]. In details, CPE_{film} and R_{film} are related to the dielectric properties and resistivity of the film and C_{dl} represents the double-layer capacitance. The two essential elements, R_p and R_s, reflect the reaction kinetics at the interface and specifically, R_p reflects the total charge transfer resistance and R_s is related to the resistance of surface intermediates. CPE_ϕ is used to correct for relaxation of charges of the intermediates. On this basis, the *operando* EIS is adopted to compare OER and UOR on NiFe-LDH in the low potential region (0.3–0.5 V). In the Nyquist plots (Fig. 1e and f), the $C_{film}R_{film}$ loop of NiFe-LDH is not clearly observed for both OER and UOR and therefore, the resistance at high frequencies is mainly ascribed to the solution resistance (R_Ω), which is determined to be about 1.6 Ω in both electrolytes. Hence, the electrolyte resistance may be independent of urea addition. On the other hand, the typical semicircle emerges and narrows with increasing potentials suggesting accelerated charge transfer. In the Bode-phase plots (Fig. 1g and h), we divide the two regions to reflect Ni cations (intermediate-frequency region) and water or urea (low-frequency region) electro-oxidization. Generally, the smaller drop in the phase angle indicates faster electron transfer. In the OER electrolyte, the diminishing trend of the phase angle in the low-frequency region is consistent with that in the intermediate-frequency region. As a result, R_p decreases with decreasing $CPE_\phi R_s$ revealing that OER commences due to accumulation of intermediates. On the other hand, in the UOR electrolyte, the phase angle in the intermediate-frequency region is relatively stable despite a drastic drop in the low-frequency region. The phenomenon is different from that observed from α-$Ni(OH)_2$ [8] and β-$Ni(OH)_2$ [7], both of which show phase angle decrease in the intermediate-frequency region as the potentials go up reflecting that the initial activity is related to dehydrogenation of $Ni(OH)_6$ octahedrons. Therefore, it is reasonable to infer that UOR on NiFe-LDH in the low potential region is based on a direct electron transfer mechanism that possibly utilizes absorbed oxygen on the Fe sites.

3.3. Active sites in the high potential region

When the applied potential is larger than 0.5 V, the phase angle in the intermediate-frequency region starts to drop and $Ni^{2+\delta}O_xH_y$ is formed (Fig. S4). To understand the reaction mechanism in the high potential region, we compare the CV activation process of pristine NiFe-LDH in different potential regions (potentials terminated before and after the Ni oxidization threshold). As shown in Fig. 2a, if the potential range (0–0.5 V) does not exceed the threshold of Ni oxidization, there is no apparent activation in the 20 CV scans and the reaction current in the forward sweep is larger than that in the backward scan. In contrast, the activation phenomenon appears and the backward current is larger if the potential range (0–0.7 V) includes the Ni oxidization threshold.

The larger backward current should result from spontaneous consumption of accumulated $Ni^{2+\delta}O_xH_y$ in the forward sweep. To validate the spontaneity, we acquire time-varying Raman scattering spectra from NiFe-LDH in the UOR and OER electrolytes at 0 and 30 min after terminating the operation at 0.6 V (keep 10 min). As shown in Fig. 2b, the lattice modes of $Ni^{2+\delta}O_xH_y$ disappear and the original signals of NiFe-LDH recover immediately as soon as the high UOR voltage is cut off. Conversely, the evolved $Ni^{2+\delta}O_xH_y$ phase is maintained for at least 30 min after the OER voltage is turned off. Our previous work shows that consumption of the derivative $Ni^{2+\delta}O_xH_y$ phase of α-$Ni(OH)_2$ by urea needs around 5 h [8]. Accordingly, the fast reaction kinetics can be explained by that UOR proceeding on NiFe-LDH in the high potential region depends on the electrophilic lattice oxygen of $Ni^{2+\delta}O_xH_y$ and active sites regeneration. On the other hand, although the average valance state of Ni is between 3.3 and 3.7 in the $Ni(OH)_2$ derived $Ni^{2+\delta}O_xH_y$ [26], Lewis acid Fe^{3+} incorporation may increase the acidity of –OH moieties of Ni, resulting in easier generation of Ni^{4+} sites and higher oxidizing ability [25,34]. Moreover, fast active site regeneration

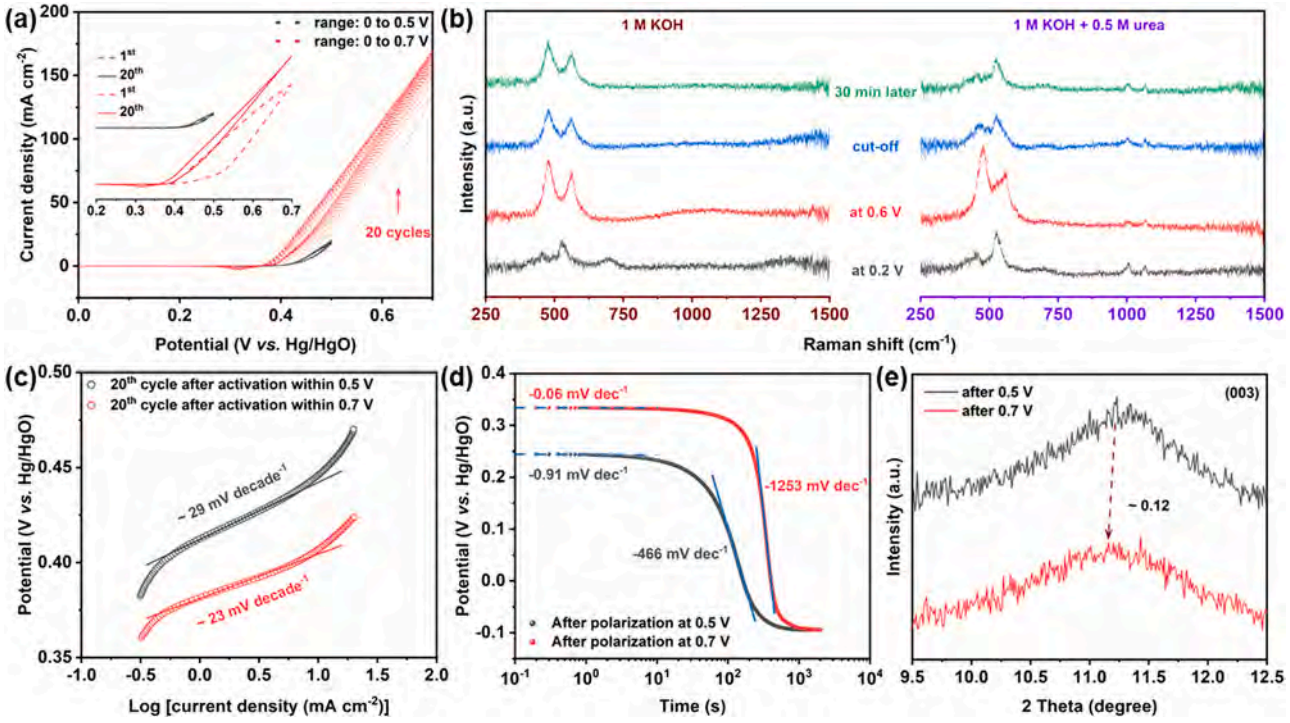

Fig. 2. (a) CV curves showing the activation processes of NiFe-LDH in different ranges (inset showing comparing the 1st and 20th cycles for different activation ranges); (b) Raman scattering spectra of wet NiFe-LDH during operation and after the potential ceases in the OER and UOR electrolytes; (c) Tafel curves obtained from the forward sweep of the 20th cycle; (d) OCP decay against log(time) after polarization for 200 s at 0.5 V and 0.7 V; (e) (003) diffraction peak of wet NiFe-LDH after polarization for 30 min polarization at 0.5 V and 0.7 V.

due to the strong oxidizing ability may partially suppress the formation of OER intermediates to account for the passivation-free phenomenon on the NiFe-LDH electrode as mentioned above. It is believed that competing OER contributes to the current at a higher potential (above 0.9 V) as evidenced by the emergence of a broad band between 850 and 1200 cm^{-1} in the *operando* Raman spectra above 0.9 V reflecting O–O^- stretching of active oxygen species, which is the typical signal of OER intermediates (Fig. S5a) [35,36]. In comparison, the O–O^- stretching mode emerges when the OER occurs in the urea-free electrolyte (Fig. S5b).

3.4. Increased active sites in the high potential region

Despite the activity improvement at high potentials shown by the CV curves after activation in different ranges, the Tafel slopes obtained from the *iR* corrected forward sweeps show similar values (below 30 mV $decade^{-1}$, Fig. 2c) at low potentials, implying that the activity improvement originates from not only the high valance Ni, but also more active sites [37,38]. Because of the dynamic surface with potentials, the OCP decay is measured to track the active sites. Generally, the OCP decay is measured after electrode polarization at a potential where the Tafel behavior occurs. In our experiments, the polarization duration is 200 s and it is believed that the steady-state current is achieved before the OCP decay test (Fig. S6). The polarization potentials are set as 0.5 V and 0.7 in comparing UOR in the low and high potential regions, respectively. As shown in Fig. 2d, the OCP vs. *log (t)* decay curves obtained after polarization at 0.5 V and 0.7 V exhibit two linear regions and the slopes are determined. In theory, if the electrode surface capacitance is constant during OCP decay, the rate of the self-discharging process can be governed by the anodic reaction and the OCP decay curve can be written as:

$$\eta_t = \frac{2.303RT}{\beta F}\log\left(\frac{RT}{\beta F i_0}\right) - \frac{2.303RT}{\beta F}\log(t), \quad (1)$$

where β represents the transfer coefficient and the others variables have their usual meanings [38]. Consequently, the curve slopes (potential against log*t*.) should be equal to the Tafel slope (2.303RT/βF) theoretically and the experimental difference is interpreted by the surface capacity. The relationship between the true decay slope (b_{ocp}) and Tafel slope (b) is:

$$b_{ocp} = \frac{b'b}{b - b'}, \quad (2)$$

where b' is the multiple or fraction of RT/F [39]. Taking anodic UOR into consideration, the small slope in the initial linear region (several seconds) indicates that the surface capacity increases with decreasing potential due to the larger charged surface coverage of intermediates [38]. After the release and low coverage of intermediates due to self-discharging, the surface capacity decreases with decreasing potential as manifested by a greater decay slope (latter liner region). Specifically, the decay slopes for a short time after 0.7 V is one-fifteenth as that after 0.5 V, indicating a high proportional coverage of charged intermediates and therefore, the active sites increase after polarization in the high potential region. For a long time, the fast self-discharging of large amounts of intermediates and charged surface groups may account for the bigger slope after 0.7 V polarization, which supports the postulate that the derivative $Ni^{2+\delta}O_xH_y$ phase spontaneously sequesters protons and electrons of urea molecules.

To reveal the origin of the increasing active sites, we carry out post-mortem *quasi-operando* small-angle X-ray diffraction (XRD) to monitor the interlayer distance. As shown in Fig. 2e, the typical interlayer peak of (003) shows about a 0.12° red-shift after 30 min at 0.7 V in UOR compared to 0.5 V. Accordingly, it is reasonable to conjecture that electrolyte penetration into the interlayer region is related to Ni oxidization and the increasing active sites stem from oxidization of internal atoms. The results support the reasoning that the internal atoms in NiFe-LDH contribute to the catalytic activity [37], but it must be emphasized that the contribution depends on the driving potentials.

3.5. Plasma processing

According to the mechanisms described above, a straightforward strategy to improve the UOR activity of NiFe-LDH is to lower the voltage to generate the $Ni^{2+\delta}O_xH_y$ phase to activate more active sites and improve the oxidization ability. It has been reported that the unsaturated coordinated atoms of $Ni(OH)_2$ slabs, especially the four-coordinated Ni at the edge, have a lower OH^- absorption energy because of the more positive charge states leading to the preferential oxidization [40,41]. Here, plasma processing is performed to produce NiFe-LDH slab reconstruction to form an edge-rich structure that can easily generate the $Ni^{2+\delta}O_xH_y$ phase to improve the UOR activity.

The initial thin NiFe-LDH nanosheets mentioned above are synthesized hydrothermally and the surface morphology is characterized by scanning electron microscopy (SEM) and transmission electron microscopy (TEM). Fig. 3a and b show the vertically aligned NiFe-LDH nanosheets revealing that the film is composed of aligned NiFe-LDH nanosheets uniformly distributed on the Ni foam. The edge thickness is between 5 and 20 nm according to SEM and TEM (Fig. 3b and S7), indicating that the initial nanosheets contain 6–26 layers (interlayer distance: ~ 0.767 nm). In Ar plasma-induced layer reconstruction, the thickness of the nanosheets can be controlled by the processing time. As shown in Fig. 3a-h, the thickness changes with time and is larger than 80 nm (about 104 layers) for a processing time of 60 min. It is conjectured the NiFe-LDH nanosheets experience diffusion, recombination, and layer restacking in the high-energy Ar-plasma environment as shown in Fig. 3i, whereas Ni, Fe, and O atoms rearrange into a rhombohedral layered structure with the *R3m* space group.

The samples designated by the processing time are assessed by CV. After activation, the four electrodes show nearly identical onset potentials and reaction kinetics in OER in 1 M KOH (Fig. S8), indicating similar activity. However, the small shoulder peak before OER shifts with processing time suggesting that Ni oxidization is marginally easier for the thicker multilayer NiFe-LDH sheets. Meanwhile, the OER activity on NiFe-LDH is independent of the thickness of the layers and threshold of Ni oxidization, thereby supporting the previous assertion that high valance Fe sites in NiFe-LDH serve as the active sites in OER [35,36,42,43]. In contrast, different UOR activities are exhibited when the electrodes are immersed in 1 M KOH with 0.5 M urea. As shown in Fig. 4a, the NiFe-LDH-40 electrode shows the highest catalytic activity, requiring 0.389 V and 0.437 V for densities of 10 mA cm^{-2} and 100 mA $cm^{-2,}$ respectively, which is superior to that of NiFe-LDH-0. It is noted that all the plasma treated electrodes are better than the untreated one, suggesting that the UOR mechanism is different from that of OER and confirming the effectiveness of plasma-induced reconstruction. The Nyquist plots in Fig. 4b indicate almost the same ohmic resistance at high frequencies, thus eliminating the effects of resistance on the activity. The charge transfer rates reflected by the semicircle diameters exhibit the same trend as the CV curves corroborating that NiFe-LDH-40 has the fastest kinetics. In the Bode-phase plots (inset in Fig. 4b), the plasma processed samples show smaller phase angles than the untreated one in the intermediate frequency region and therefore, plasma processing lowers the oxidization energy barriers of Ni.

Because of the dynamic surface, it is not accurate to use the electrochemical surface area (ECSA) assessed by the double-layer capacitance (C_{dl}) to infer the active site. Therefore, the OCP decay after polarization at 0.7 V is monitored to study the active sites at high potentials. As shown in Fig. 4c, the OCP decay curve of NiFe-LDH-40 shows the same slope as NiFe-LDH-0 after a short time, indicating similar coverage by intermediates. However, for a long time, the slope of NiFe-LDH-40 is nearly 1.43 times larger than that of NiFe-LDH-0, suggesting higher proportional coverage of charged groups on NiFe-LDH-40 at

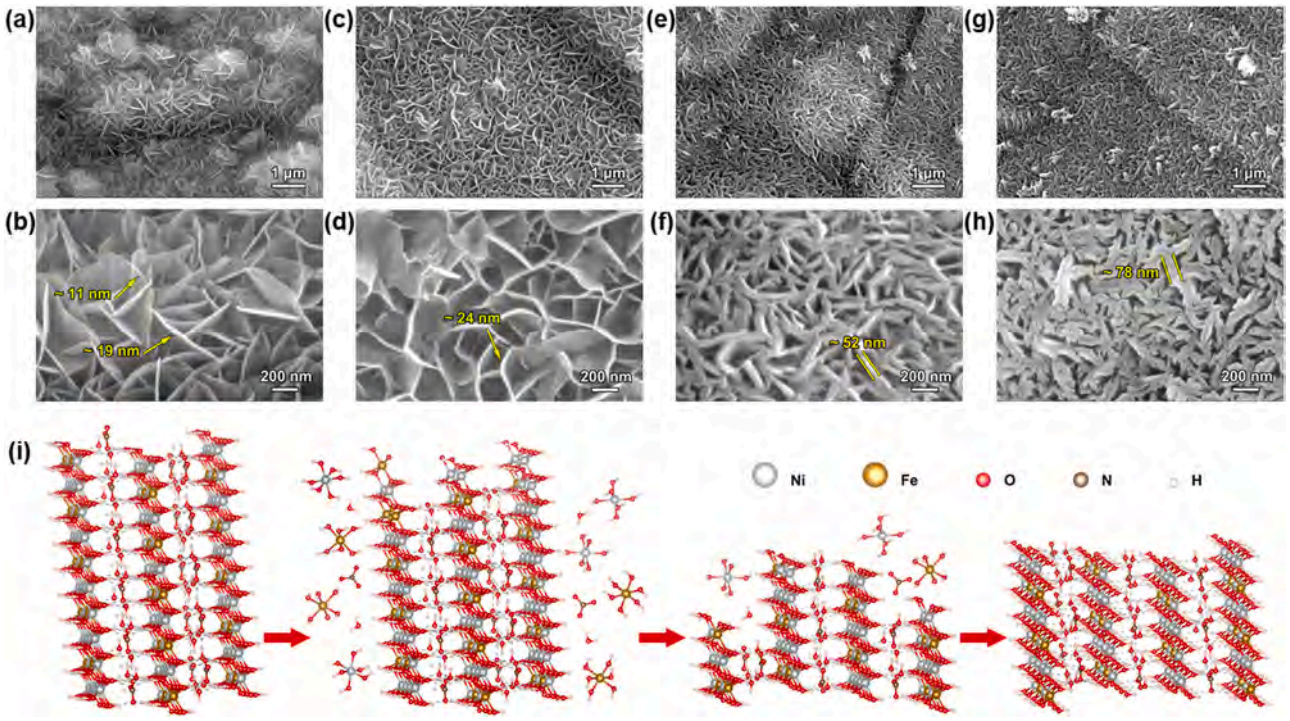

Fig. 3. SEM images of (a, b) NiFe-LDH-0, (c, d) NiFe-LDH-20, (e, f) NiFe-LDH-40, (g, h) NiFe-LDH-60; (i) Schematic of the layer reconstruction process of NiFe-LDH during Ar plasma treatment.

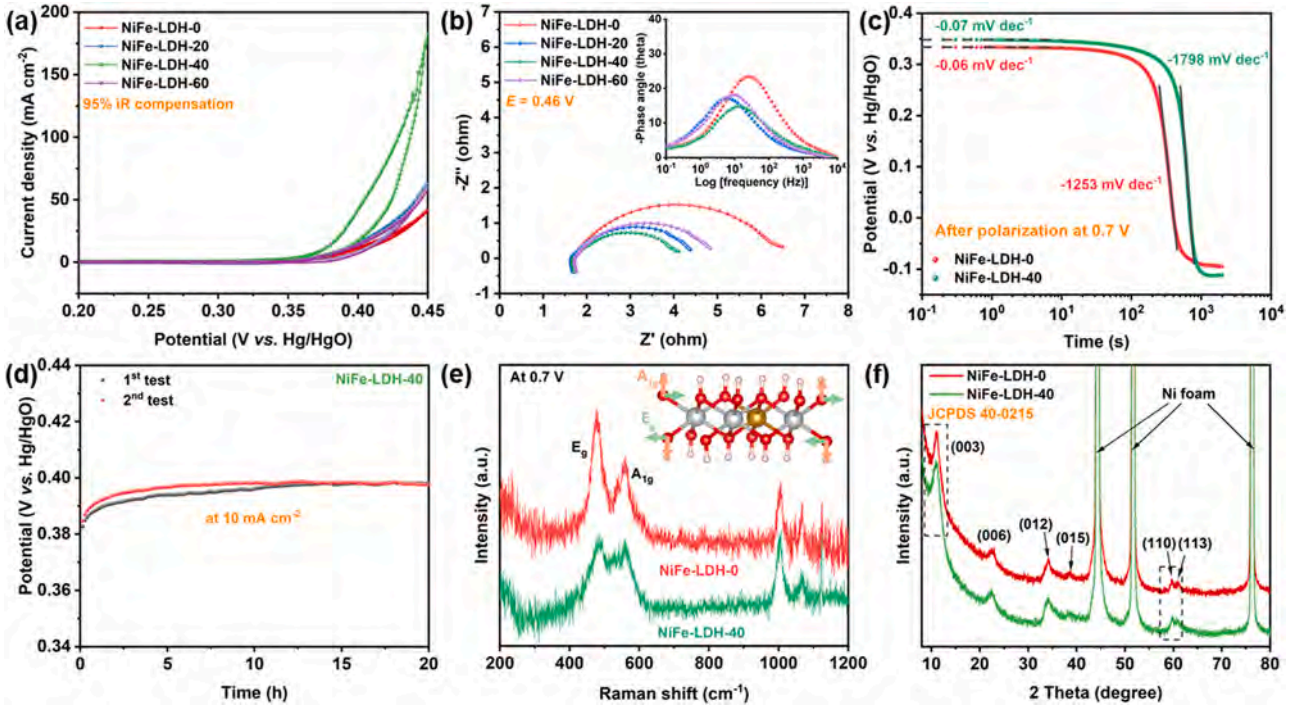

Fig. 4. (a) IR corrected CV curves and (b) Nyquist plots (inset showing the corresponding Bode-phase plots) of the four electrodes; (c) OCP decay versus log(time) after polarization for 200 s at 0.7 V for NiFe-LDH-0 and NiFe-LDH-40; (d) Two consecutive chronopotentiometry runs at 10 mA cm^{-2} of NiFe-LDH-40; (e) O*perando* Raman scattering spectra at 0.7 V of NiFe-LDH-0 and NiFe-LDH-40 in the UOR electrolyte (inset showing the vibration modes of $A_{1\,g}$ and E_g); (f) XRD patterns of NiFe-LDH-0 and NiFe-LDH-40.

0.7 V. The stability of NiFe-LDH-40 is evaluated by conducting two consecutive chronopotentiometry tests at 10 mA cm^{-2}. As shown in Fig. 4d, there is an approximately a 10-mV voltage increase in the 20-h test but the performance recovers in the fresh electrolyte, consequently validating the superior stability.

To further understand the improvement and mechanism, surface evolution of NiFe-LDH-40 is investigated by *operando* Raman scattering. As shown in the Raman spectra (Fig. S9), the phase transition voltage of NiFe-LDH-40 is determined at about 0.5 V (20 mV cathodic shift relative to NiFe-LDH-0) indicative of a smaller driven force of Ni oxidization.

After the formation of $Ni^{2+\delta}O_xH_y$, the intensity ratio of the Ni–O E_g and $A_{1\,g}$ modes (bending and stretching vibrations, I_B/I_S) is different for the two electrodes. For instance, I_B/I_S derived from NiFe-LDH-40 is less than that of NiFe-LDH-0 at 0.7 V (Fig. 4e). Generally, the E_g and $A_{1\,g}$ modes are related to oxygen atoms vibrating along adjacent O-layers in the *ab* plane and along the *c*-axis, respectively, as shown in the inset in Fig. 4e. Accordingly, a smaller I_B/I_S ratio is associated with larger polarizability of the $A_{1\,g}$ mode because there are more reconstructed slabs in NiFe-LDH-40. As a result, the different electron cloud distribution along the *c*-axis may reflect the existence of structural disorder, particularly stacking faults of new layers [36,44]. The results impart valuable information to track the larger proportion of charged groups in the high potential region.

XRD, X-ray photoelectron spectroscopy (XPS), and Raman scattering are conducted to determine the difference between the pristine NiFe-LDH-0 and NiFe-LDH-40. The XRD patterns (Fig. 4f) can be indexed to the typical layered double hydroxide structure of binary NiFe (JDPDS 40–0215) showing that the structure is preserved after plasma processing, although some peaks such as (003) and (110) are slightly broader. It can be interpreted as follows. The concentrations of interlayer anions are different in the new and original layers, leading to fluctuating interlayer spacing [45]. Furthermore, as shown by the Raman spectra, stacking faults may be responsible since the disorder is only along the *c*-axis and the order within the *ab*-plane is unaffected [46,47]. In the XPS data (Fig. S10), both samples show the typical NiFe-LDH signals, including the primary Ni^{2+} peak at 855.4 eV and small amount of Ni^{3+} at 856.6 for Ni $2p_{3/2}$, Fe^{3+} at 713.0 eV for Fe $2p_{3/2}$, and –OH at 531.2 eV for O 1 *s* [48,49]. The atomic ratios of Ni to Fe are about 2.6 and 2.8 for NiFe-LDH-0 and NiFe-LDH-40, respectively, thus eliminating the effects of the structure and catalytic activity stemming from the elemental contents. We have also found no direct evidence to claim the large proportion of defects (either anion or cation vacancies) is sufficient to affect the average valence state. Hence, the Ni or Fe atoms with high mobility and reconstruction ability recombine in the new layers in the Ar plasma. Although the reconstructed layers may rotate and translate due to the weak bonds between the layers, most internal atoms are defect-free [27]. On the other hand, the counteracting dependence of anions and cations may balance the average valance states because of the complicated interactions between the plasma and materials. Even so, we still notice that the broader shoulder of NiFe-LDH-40 in the Raman scattering spectra (Fig. S11) may reflect different phonon properties resulting from the complex coordination environment and more edge exposure.

3.6. Urea-assisted hydrogen generation

To demonstrate the practicality as well as advantages such as energy saving, a commonly used alkaline urea-assisted hydrogen generation electrolyzer composed of the plasma-processed Ni foam electrode and NiFe-LDH-40 electrode as the cathode and anode, respectively, is assembled (Fig. 5a). Our pre-experiments show that the alkaline hydrogen evolution reaction (HER) activity on the plasma-processed Ni foam electrode is similar to that on the NiFe-LDH-40 and independent of urea addition (Figs. S12 and S13), but the UOR activities on Ni foam and plasma-processed Ni foam are not satisfactory (Fig. S14). As shown in Fig. 5b, the UOR-coupled hydrogen generation device requires 1.72 V and 1.892 V for 100 cm^{-2} and 300 mA cm^{-2}, respectively, which are 76 mV and 90 mV lower than those of the overall water-splitting device. Of particular importance, despite the excellent activity of conventional anodic $Ni(OH)_2$ electrode in the low potential region, inevitable passivation occurs near 1.73 V in the UOR-assisted hydrogen generation device. The overall current density drops below that of the NiFe-LDH-40 assembled system after 1.793 V (Fig. 5c). Further comparison of the three systems is shown in Fig. 5d, which reveals the lowest potential at 300 mA cm^{-2} and largest current density at 1.9 V, confirming the advantages of the NiFe-LDH-40 anode, especially from the perspective of lessened energy depletion. The operation stability is assessed by three consecutive experiments (6 h) at 2.8 V. As shown in Fig. 5e, although there is a 40-mA cm^{-2} drop during each test, the performance nearly recovers in the new test. Considering that the urea concentration decreases gradually under high potential conditions, the catalyst is robust, stable, and durable. In addition, the XPS results obtained from NiFe-

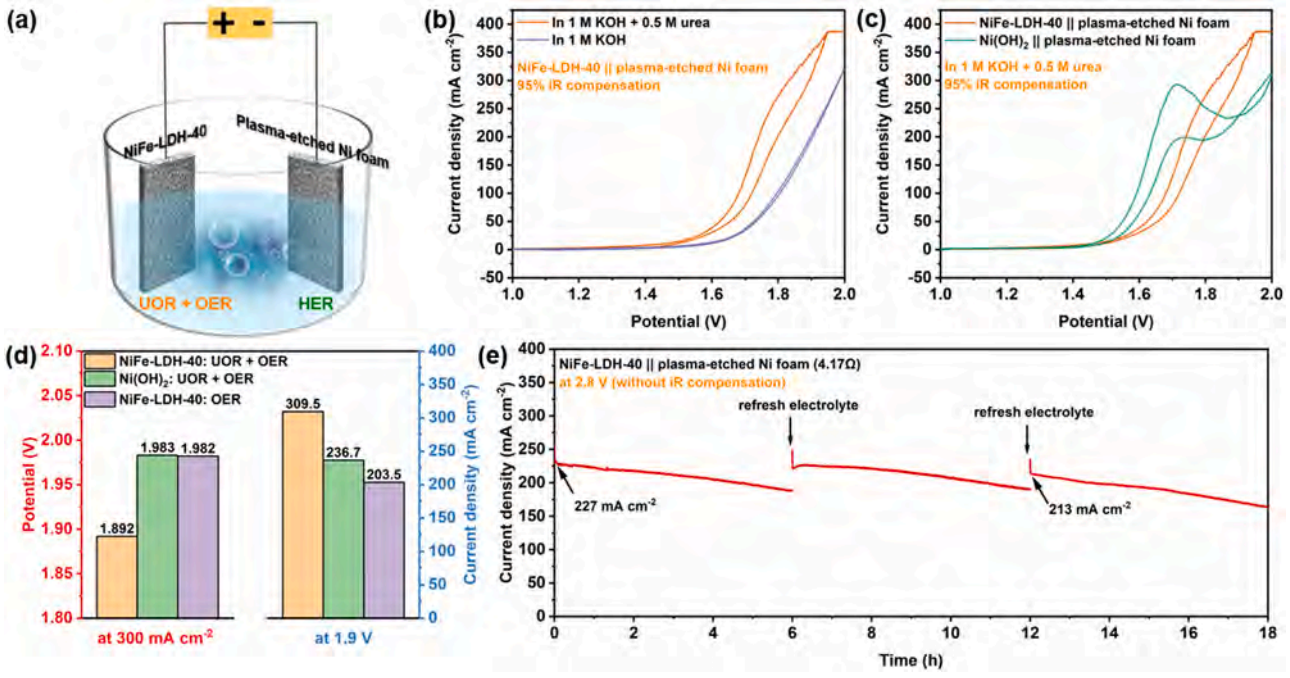

Fig. 5. (a) Schematic of the urea-assisted hydrogen generation device; (b) CV curves of the urea-assisted water electrolysis and alkaline water electrolysis setup with the NiFe-LDH and plasma-etched Ni foam as the anode and cathode, respectively; (c) CV curves of the urea-assisted electrolysis setup with the NiFe-LDH anode and Ni $(OH)_2$ anode; (d) Comparison of the cell voltages at 300 mA cm^{-2} and current densities at 1.9 V of the three systems; (e) Three consecutive long-term stability tests of the urea-assisted hydrogen generation cell at 2.8 V.

LDH-40 after the stability test (Fig. S15) disclose similar chemical information as the pristine one, further confirming the stability and validating the postulate that the $Ni^{2+\delta}$ can be quickly reduced by urea after power dump.

4. Conclusions

The UOR characteristics and active sites of NiFe-LDH self-anchored on the Ni foam are determined in the low and high potential regions. UOR occurs on NiFe-LDH before OER and the reaction can occur on both the pristine NiFe-LDH and derivative $Ni^{2+\delta}O_xH_y$ phase with different active sites. UOR on NiFe-LDH in the high potential region depends on the strong oxidization ability of the derivative $Ni^{2+\delta}O_xH_y$ and regeneration of active sites mechanism, giving rise to fast reaction kinetics and co-occurrence of UOR and OER. Moreover, a high potential can activate the internal atoms to participate in the reaction, consequently increasing the active sites and improving the properties. Ar plasma processing produces layer reconstruction of NiFe-LDH so that the $Ni^{2+\delta}O_xH_y$ phase is generated more easily to boost the UOR activity. To illustrate the practicality, the assembled urea-assisted electrocatalytic hydrogen device comprising the Ar-plasma processed NiFe-LDH as the anode delivers better performance than the urea-free one including no observable passivation and appreciable energy saving.

CRediT authorship contribution statement

All authors participate in the experimental and theoretical analysis. The paper was prepared and revised mainly by D. Li and P. K. Chu.

Declaration of Competing Interest

The authors declare that they have no known competing financial interests or personal relationships that could have appeared to influence the work reported in this paper.

Data Availability

Data will be made available on request.

Acknowledgments

We acknowledge the financial support by City University of Hong Kong Strategic Research Grant (SRG) [grant number 7005505], City University of Hong Kong Donation Research Grant [grant number DON-RMG 9229021], as well as the State Key Laboratory of Powder Metallurgy of Central South University in China.

Appendix A. Supporting information

Supplementary data associated with this article can be found in the online version at doi:10.1016/j.apcatb.2022.122240.

References

[1] D. Xiao, D.-L. Bao, X. Liang, Y. Wang, J. Shen, C. Cheng, P.K. Chu, Experimental and theoretical investigation of the control and balance of active sites on oxygen plasma-functionalized MoSe2 nanosheets for efficient hydrogen evolution reaction, Appl. Catal., B 288 (2021), 119983.
[2] C. Huang, D.H. Wu, P. Qin, K. Ding, C.R. Pi, Q.D. Ruan, H. Song, B. Gao, H.Y. Chen, P.K. Chu, Ultrafine Co nanodots embedded in N-doped carbon nanotubes grafted on hexagonal VN for highly efficient overall water splitting, Nano Energy 73 (2020).
[3] B. Wang, Y.Z. Ye, L. Xu, Y. Quan, W.X. Wei, W.S. Zhu, H.M. Li, J.X. Xia, Space-confined yolk-shell construction of Fe(3)O(4)nanoparticles inside N-doped hollow mesoporous carbon spheres as bifunctional electrocatalysts for long-term rechargeable zinc-air batteries, Adv. Funct. Mater. 30 (2020).
[4] D. Li, B.W. Zhang, Y. Li, R.S. Chen, S. Hu, H.W. Ni, Boosting hydrogen evolution activity in alkaline media with dispersed ruthenium clusters in NiCo-layered double hydroxide, Electrochem. Commun. 101 (2019) 23–27.
[5] H. Sun, C.W. Tung, Y. Qiu, W. Zhang, Q. Wang, Z. Li, J. Tang, H.C. Chen, C. Wang, H.M. Chen, Atomic metal-support interaction enables reconstruction-free dual-site electrocatalyst, J. Am. Chem. Soc. 144 (2022) 1174–1186.
[6] S. Verma, S. Lu, P.J.A. Kenis, Co-electrolysis of CO_2 and glycerol as a pathway to carbon chemicals with improved technoeconomics due to low electricity consumption, Nat. Energy 4 (2019) 466–474.
[7] W. Chen, L. Xu, X. Zhu, Y.C. Huang, W. Zhou, D. Wang, Y. Zhou, S. Du, Q. Li, C. Xie, L. Tao, C.L. Dong, J. Liu, Y. Wang, R. Chen, H. Su, C. Chen, Y. Zou, Y. Li, Q. Liu, S. Wang, Unveiling the electrooxidation of urea: intramolecular coupling of the N-N bond, Angew. Chem. Int. Ed. Engl. 60 (2021) 7297–7307.
[8] D. Li, Y. Zhang, X. Zhou, C. Huang, Y. Wen, L. Liu, Q. Li, Y. Xu, Y. Wu, Q. Ruan, Y. Ma, F. Xiong, D. Xiao, P. Liu, G. Wang, B. Mehrjou, B. Wang, H. Li, R. Chen, H. Ni, Z. Zeng, P.K. Chu, Dynamic active sites on plasma engraved Ni hydroxide for enhanced electro-catalytic urea oxidation, J. Energy Chem. 71 (2022) 150–158.
[9] S.K. Geng, Y. Zheng, S.Q. Li, H. Su, X. Zhao, J. Hu, H.B. Shu, M. Jaroniec, P. Chen, Q.H. Liu, S.Z. Qiao, Nickel ferrocyanide as a high-performance urea oxidation electrocatalyst, Nat. Energy 6 (2021) 904–912.
[10] C. Tang, R. Zhang, W. Lu, Z. Wang, D. Liu, S. Hao, G. Du, A.M. Asiri, X. Sun, Energy-saving electrolytic hydrogen generation: Ni2 P nanoarray as a high-performance non-noble-metal electrocatalyst, Angew. Chem. Int. Ed. Engl. 56 (2017) 842–846.
[11] X. Liu, J. He, S. Zhao, Y. Liu, Z. Zhao, J. Luo, G. Hu, X. Sun, Y. Ding, Self-powered H2 production with bifunctional hydrazine as sole consumable, Nat. Commun. 9 (2018) 4365.
[12] Y. Liu, J. Zhang, Y. Li, Q. Qian, Z. Li, Y. Zhu, G. Zhang, Manipulating dehydrogenation kinetics through dual-doping Co3N electrode enables highly efficient hydrazine oxidation assisting self-powered H2 production, Nat. Commun. 11 (2020) 1–13.
[13] B. You, N. Jiang, X. Liu, Y. Sun, Simultaneous H2 generation and biomass upgrading in water by an efficient noble-metal-free bifunctional electrocatalyst, Angew. Chem. Int. Ed. Engl. 55 (2016) 9913–9917.
[14] W.J. Liu, Z. Xu, D. Zhao, X.Q. Pan, H.C. Li, X. Hu, Z.Y. Fan, W.K. Wang, G.H. Zhao, S. Jin, G.W. Huber, H.Q. Yu, Efficient electrochemical production of glucaric acid and H2 via glucose electrolysis, Nat. Commun. 11 (2020) 265.
[15] C. Huang, Y. Huang, C. Liu, Y. Yu, B. Zhang, Integrating hydrogen production with aqueous selective semi-dehydrogenation of tetrahydroisoquinolines over a Ni2 P bifunctional electrode, Angew. Chem. Int. Ed. Engl. 58 (2019) 12014–12017.
[16] L. Dong, G.R. Chang, Y. Feng, X.Z. Yao, X.Y. Yu, Regulating Ni site in NiV LDH for efficient electrocatalytic production of formate and hydrogen by glycerol electrolysis, Rare Met. 41 (2022) 1583–1594.
[17] L. Du, Y. Sun, B. You, Hybrid water electrolysis: replacing oxygen evolution reaction for energy-efficient hydrogen production and beyond, Mater. Rep.: Energy 1 (2021), 100004.
[18] L. Wang, Y. Zhu, Y. Wen, S. Li, C. Cui, F. Ni, Y. Liu, H. Lin, Y. Li, H. Peng, B. Zhang, Regulating the local charge distribution of ni active sites for the urea oxidation reaction, Angew. Chem. Int. Ed. Engl. 60 (2021) 10577–10582.
[19] V. Vedharathinam, G.G. Botte, Direct evidence of the mechanism for the electro-oxidation of urea on Ni(OH)(2) catalyst in alkaline medium, Electrochim. Acta 108 (2013) 660–665.
[20] D. Wang, W. Yan, G.G. Botte, Exfoliated nickel hydroxide nanosheets for urea electrolysis, Electrochem. Commun. 13 (2011) 1135–1138.
[21] L. Gao, X. Cui, C.D. Sewell, J. Li, Z. Lin, Recent advances in activating surface reconstruction for the high-efficiency oxygen evolution reaction, Chem. Soc. Rev. 50 (2021) 8428–8469.
[22] D. Zhou, P. Li, X. Lin, A. McKinley, Y. Kuang, W. Liu, W.F. Lin, X. Sun, X. Duan, Layered double hydroxide-based electrocatalysts for the oxygen evolution reaction: identification and tailoring of active sites, and superaerophobic nanoarray electrode assembly, Chem. Soc. Rev. 50 (2021) 8790–8817.
[23] J.F. Xie, H.C. Qu, F.C. Lei, X. Peng, W.W. Liu, L. Gao, P. Hao, G.W. Cui, B. Tang, Partially amorphous nickel-iron layered double hydroxide nanosheet arrays for robust bifunctional electrocatalysis, J. Mater. Chem. A 6 (2018) 16121–16129.
[24] H.C.A. Sun, W. Zhang, J.G. Li, Z.S. Li, X. Ao, K.H. Xue, K.K. Ostrikov, J. Tang, C. D. Wang, Rh-engineered ultrathin NiFe-LDH nanosheets enable highly-efficient overall water splitting and urea electrolysis, Appl. Catal. B-Environ. 284 (2021).
[25] Z. Qiu, C.W. Tai, G.A. Niklasson, T. Edvinsson, Direct observation of active catalyst surface phases and the effect of dynamic self-optimization in NiFe-layered double hydroxides for alkaline water splitting, Energy Environ. Sci. 12 (2019) 572–581.
[26] S. Klaus, Y. Cai, M.W. Louie, L. Trotochaud, A.T. Bell, Effects of Fe electrolyte impurities on Ni(OH)(2)/NiOOH structure and oxygen evolution activity, J. Phys. Chem. C. 119 (2015) 7243–7254.
[27] D.S. Hall, D.J. Lockwood, C. Bock, B.R. MacDougall, Nickel hydroxides and related materials: a review of their structures, synthesis and properties, P R. Soc. a-Math. Phy 471 (2015), 20140792.
[28] Y. Luo, Y. Wu, D. Wu, C. Huang, D. Xiao, H. Chen, S. Zheng, P.K. Chu, NiFe-layered double hydroxide synchronously activated by heterojunctions and vacancies for the oxygen evolution reaction, Acs Appl. Mater. Inter 12 (2020) 42850–42858.
[29] L.C. Bai, S.W. Lee, X.L. Hu, Spectroscopic and electrokinetic evidence for a bifunctional mechanism of the oxygen evolution reaction**, Angew. Chem. Int Ed. 60 (2021) 3095–3103.
[30] B.S. Yeo, A.T. Bell, In Situ raman study of nickel oxide and gold-supported nickel oxide catalysts for the electrochemical evolution of oxygen, J. Phys. Chem. C. 116 (2012) 8394–8400.
[31] M.W. Louie, A.T. Bell, An investigation of thin-film Ni-Fe oxide catalysts for the electrochemical evolution of oxygen, J. Am. Chem. Soc. 135 (2013) 12329–12337.

[32] R.L. Doyle, M.E.G. Lyons, Kinetics and mechanistic aspects of the oxygen evolution reaction at hydrous iron oxide films in base, J. Electrochem. Soc. 160 (2013) H142–H154.
[33] M.E.G. Lyons, M.P. Brandon, The significance of electrochemical impedance spectra recorded during active oxygen evolution for oxide covered Ni, Co and Fe electrodes in alkaline solution, J. Electroanal. Chem. 631 (2009) 62–70.
[34] N. Li, D.K. Bediako, R.G. Hadt, D. Hayes, T.J. Kempa, F. von Cube, D.C. Bell, L. X. Chen, D.G. Nocera, Influence of iron doping on tetravalent nickel content in catalytic oxygen evolving films, P Natl. Acad. Sci. USA 114 (2017) 1486–1491.
[35] S. Lee, K. Banjac, M. Lingenfelder, X. Hu, Oxygen isotope labeling experiments reveal different reaction sites for the oxygen evolution reaction on nickel and nickel iron oxides, Angew. Chem. Int. Ed. Engl. 58 (2019) 10295–10299.
[36] S. Lee, L. Bai, X. Hu, Deciphering iron-dependent activity in oxygen evolution catalyzed by nickel-iron layered double hydroxide, Angew. Chem. Int. Ed. Engl. 59 (2020) 8072–8077.
[37] R. Chen, S.F. Hung, D. Zhou, J. Gao, C. Yang, H. Tao, H.B. Yang, L. Zhang, L. Zhang, Q. Xiong, H.M. Chen, B. Liu, Layered structure causes bulk NiFe layered double hydroxide unstable in alkaline oxygen evolution reaction, Adv. Mater. 31 (2019), e1903909.
[38] R.L. Doyle, I.J. Godwin, M.P. Brandon, M.E. Lyons, Redox and electrochemical water splitting catalytic properties of hydrated metal oxide modified electrodes, Phys. Chem. Chem. Phys. 15 (2013) 13737–13783.
[39] B. Conway, P. Bourgault, Significance of emf decay measurements. Applications to the nickel oxide electrode, Trans. Faraday Soc. 58 (1962) 593–607.
[40] X.P. Wang, H.J. Wu, S.B. Xi, W.S.V. Lee, J. Zhang, Z.H. Wu, J.O. Wang, T.D. Hu, L. M. Liu, Y. Han, S.W. Chee, S.C. Ning, U. Mirsaidov, Z.B. Wang, Y.W. Zhang, A. Borgna, J. Wang, Y.H. Du, Z.G. Yu, S.J. Pennycook, J.M. Xue, Strain stabilized nickel hydroxide nanoribbons for efficient water splitting, Energy Environ. Sci. 13 (2020) 229–237.
[41] X. Wang, S. Xi, W.S.V. Lee, P. Huang, P. Cui, L. Zhao, W. Hao, X. Zhao, Z. Wang, H. Wu, H. Wang, C. Diao, A. Borgna, Y. Du, Z.G. Yu, S. Pennycook, J. Xue, Materializing efficient methanol oxidation via electron delocalization in nickel hydroxide nanoribbon, Nat. Commun. 11 (2020) 4647.
[42] J.Y. Chen, L. Dang, H. Liang, W. Bi, J.B. Gerken, S. Jin, E.E. Alp, S.S. Stahl, Operando analysis of NiFe and Fe oxyhydroxide electrocatalysts for water oxidation: detection of Fe(4)(+) by mossbauer spectroscopy, J. Am. Chem. Soc. 137 (2015) 15090–15093.
[43] M.B. Stevens, C.D.M. Trang, L.J. Enman, J. Deng, S.W. Boettcher, Reactive Fe-Sites in Ni/Fe (Oxy)hydroxide are responsible for exceptional oxygen electrocatalysis activity, J. Am. Chem. Soc. 139 (2017) 11361–11364.
[44] E. Flores, P. Novak, E.J. Berg, In situ and operando raman spectroscopy of layered transition metal oxides for li-ion battery cathodes, Front. Energy Res. 6 (2018) 16.
[45] Z.G. Zhang, H. Huo, L.G. Wang, S.F. Lou, L.Z. Xiang, B.X. Xie, Q. Wang, C.Y. Du, J. J. Wang, G.P. Yin, Stacking fault disorder induced by Mn doping in Ni(OH)(2) for supercapacitor electrodes, Chem. Eng. J. 412 (2021).
[46] C. Delmas, C. Tessier, Stacking faults in the structure of nickel hydroxide: a rationale of its high electrochemical activity, J. Mater. Chem. 7 (1997) 1439–1443.
[47] C. Tessier, P.H. Haumesser, P. Bernard, C. Delmas, The structure of Ni(OH)(2): From the ideal material to the electrochemically active one, J. Electrochem. Soc. 146 (1999) 2059–2067.
[48] X.F. Chen, D. Li, Y. Li, W.T. Zhan, C. Huang, R.S. Chen, W. Wang, H.W. Ni, P. K. Chu, Short-brush NiFeOxHy films and the Pt derivative as high-performance electrode materials for efficient electrocatalytic water splitting, Appl. Surf. Sci. 574 (2022).
[49] D. Li, X.F. Chen, Y.Z. Lv, G.Y. Zhang, Y. Huang, W. Liu, Y. Li, R.S. Chen, C. Nuckolls, H.W. Ni, An effective hybrid electrocatalyst for the alkaline HER: Highly dispersed Pt sites immobilized by a functionalized NiRu-hydroxide, Appl. Catal. B-Environ. 269 (2020).

Supporting Information

Reduced anodic energy depletion in electrocatalysis by urea and water co-oxidization on NiFe-LDH: Activity origin and plasma functionalized strategy

Dan Li[a], Xiaomin Zhou[a], Liangliang Liu[a], Qingdong Ruan[a], Xiaolin Zhang[a], Bin Wang[a], Fangyu Xiong[a], Chao Huang[a,b] *, Paul K. Chu[a] *

[a] *Department of Physics, Department of Materials Science and Engineering, and Department of Biomedical Engineering, City University of Hong Kong, Tat Chee Avenue, Kowloon, Hong Kong, China*

[b] *State Key Laboratory of Powder Metallurgy, Central South University, Changsha 410083, China*

* *Corresponding authors: chuang46-c@my.cityu.edu.hk (C. Huang); paul.chu@cityu.edu.hk (P.K. Chu)*

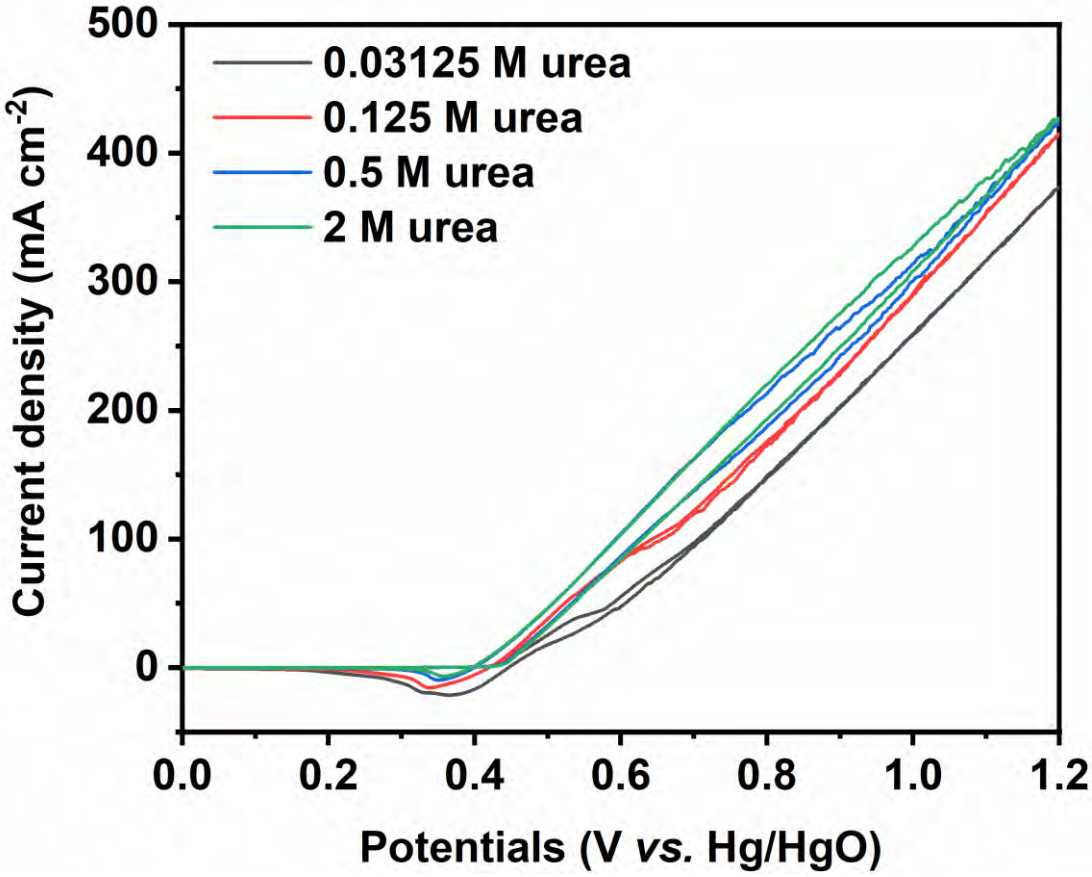

Fig. S1. Effects of the urea concentration on UOR on the NiFe-LDH electrode in 1 M KOH. The scan rate is 5 mV s^{-1}. Because of the fast UOR response, the oxidization peak of Ni ($Ni(OH)_2/Ni^{2+\delta}O_xH_y$) is almost hidden. With increasing urea concentration, the current at high potentials increases and is stable. The current increase observed up to 0.5 M may be due to the diffusion-controlled process at a low concentration. In contrast, a high concentration (2 M) has negligible effects on the current due to the kinetics limited and controlled process. The claim is supported by the cathodic peak currents which are similar for concentrations of 0.5 M and 2 M. The increase in the anodic peak current with increasing urea concentration from 0.03125 to 0.5 M stems from the high availability of urea molecules for oxidation.

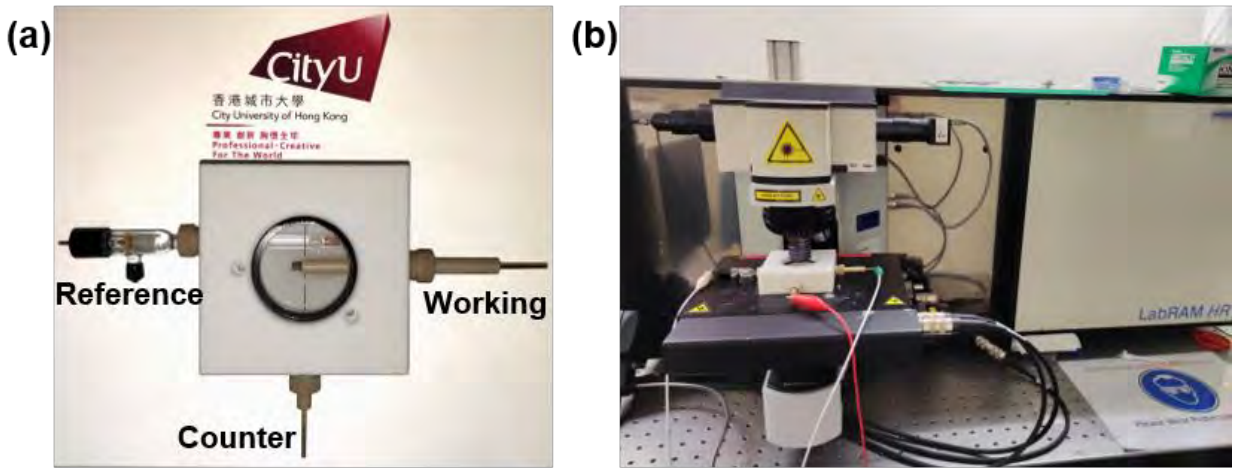

Fig. S2. (a) Photograph of the *operando* Raman cell and (b) Raman scattering instrument. The laser irradiates the electrode through the top quartz plate in the reaction.

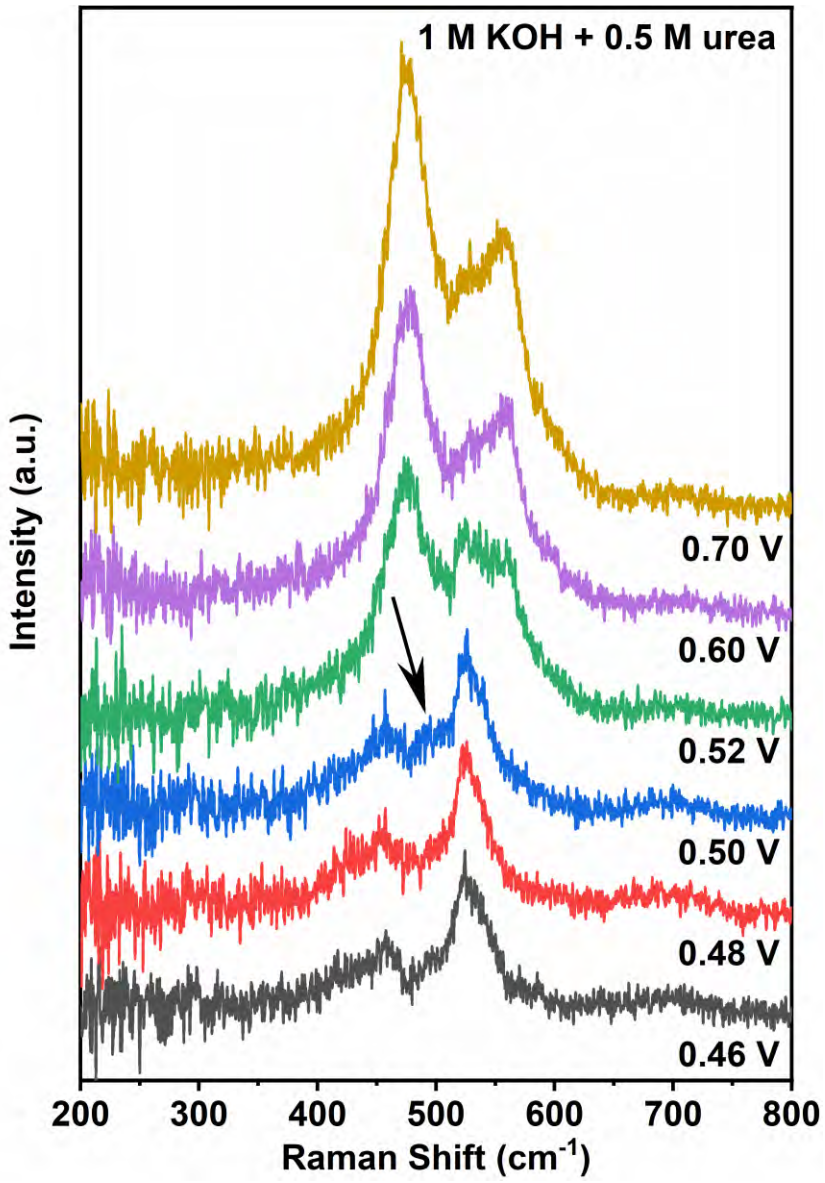

Fig. S3. *Operando* Raman spectra of NiFe-LDH in the UOR electrolyte (potentials referenced to the Hg/HgO electrode). The small peak around 495 cm^{-1} indicates the formation of $Ni(OH)_5O^-$ intermediates.

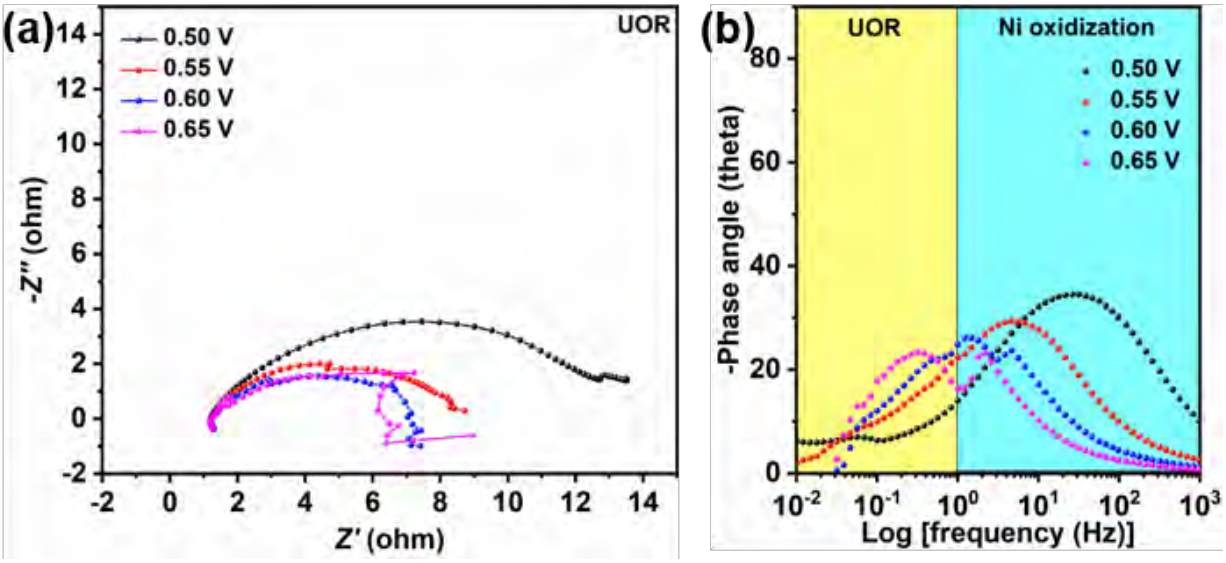

Fig. S4. (a) *Operando* Nyquist plots and (b) Bode-phase plots of NiFe-LDH at large potentials (referenced to the Hg/HgO electrode). Owing to the large current and amount of bubbles, the plots are not as smooth as those in the low potential region.

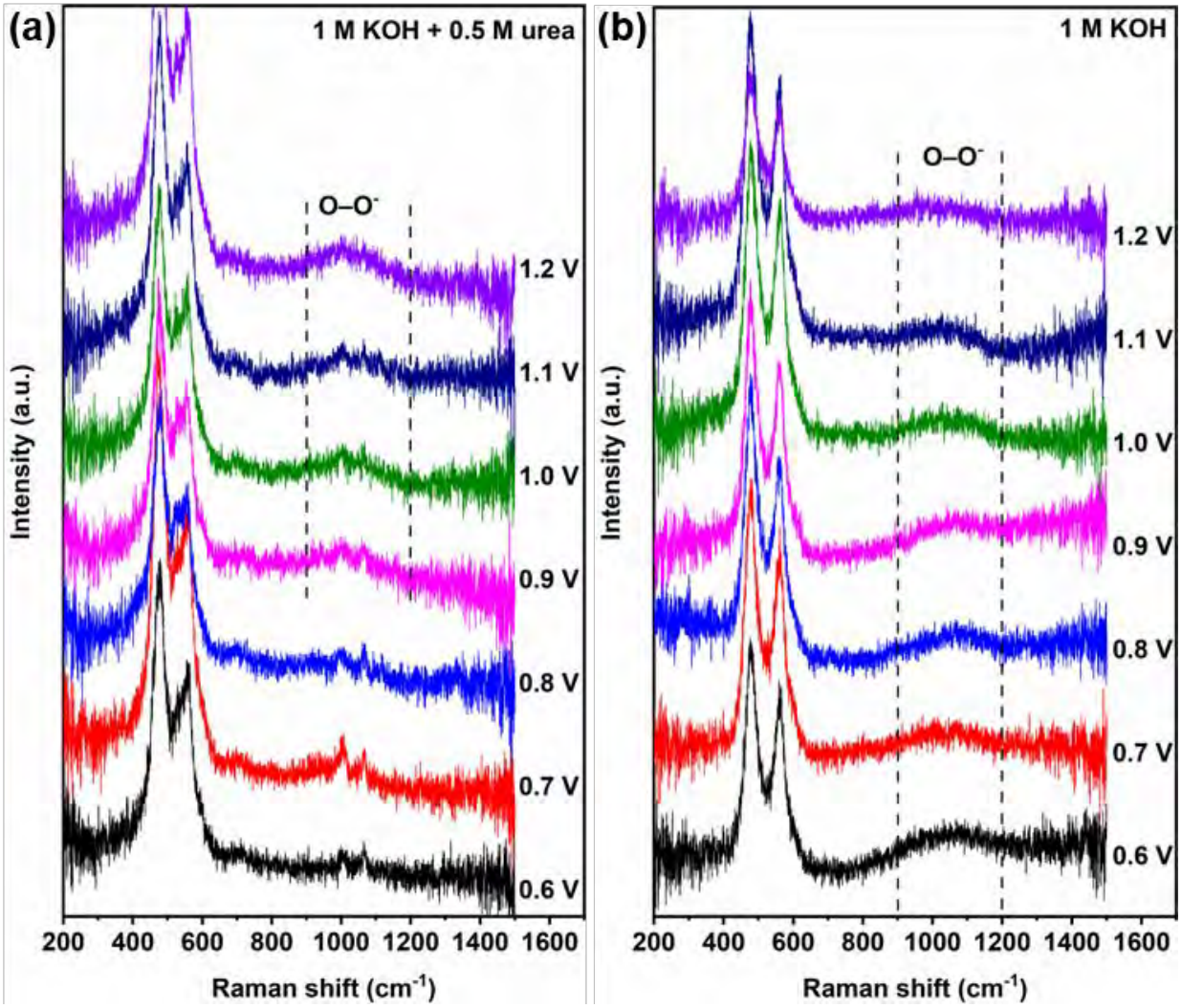

Fig. S5. *Operando* Raman spectra of NiFe-LDH: (a) UOR and (b) OER. The potentials are referenced to the Hg/HgO electrode.

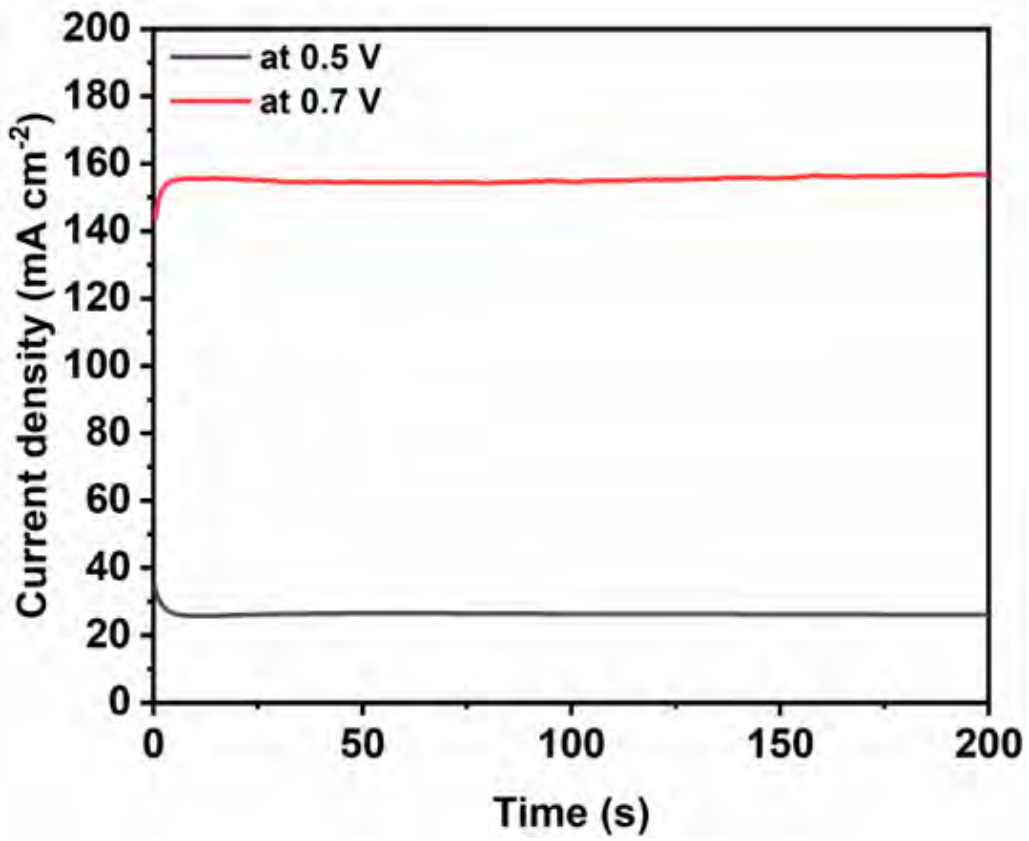

Fig. S6. Polarization curves of NiFe-LDH at 0.5 V and 0.7 V (*vs.* Hg/HgO). The current density is stable after several seconds indicating that the steady state is reached.

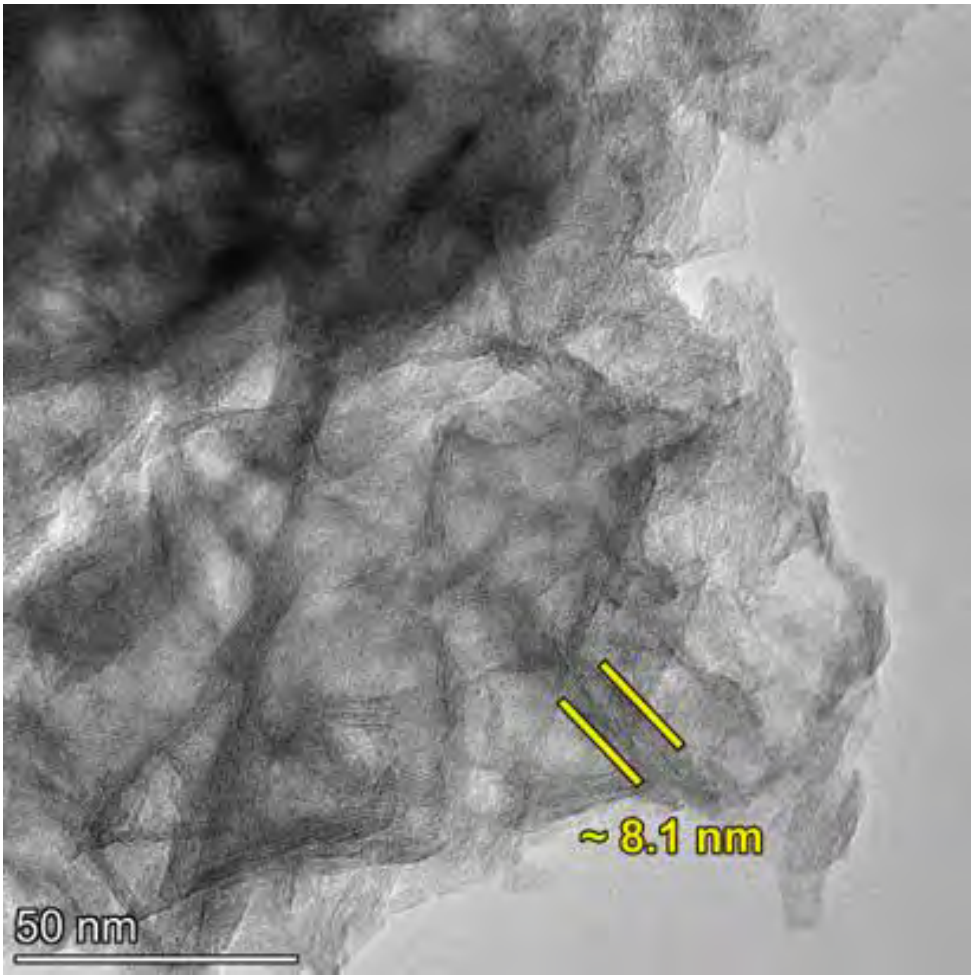

Fig. S7. TEM image of NiFe-LDH-0.

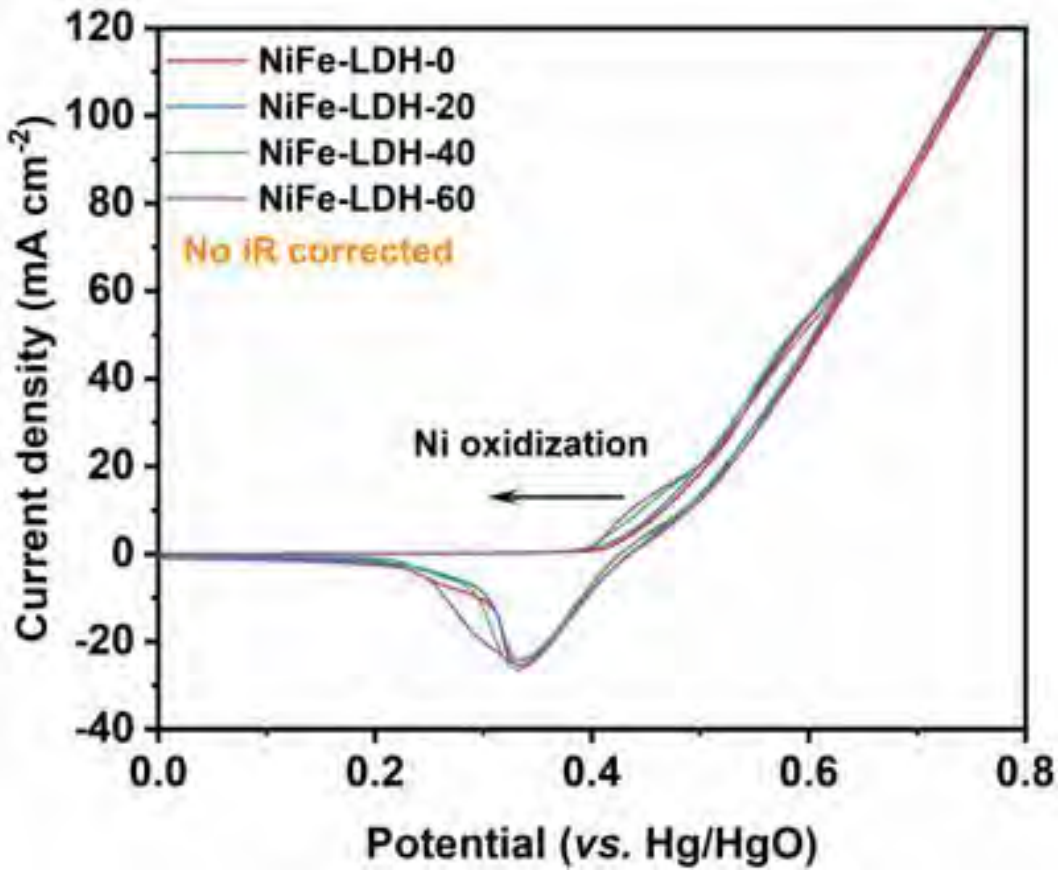

Fig. S8. CV curves of the four electrodes in the OER electrolyte.

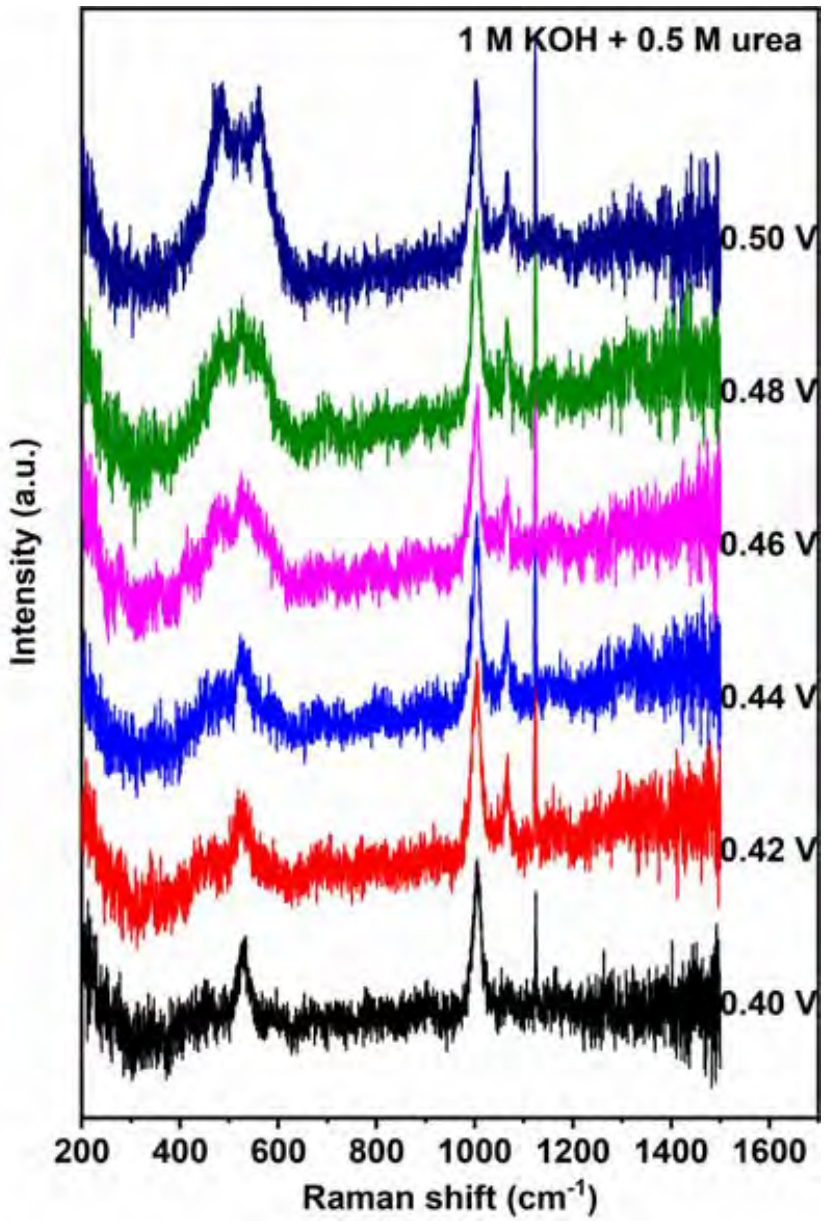

Fig. S9. *Operando* Raman scattering spectra of NiFe-LDH-40 (potentials referenced to the Hg/HgO electrode).

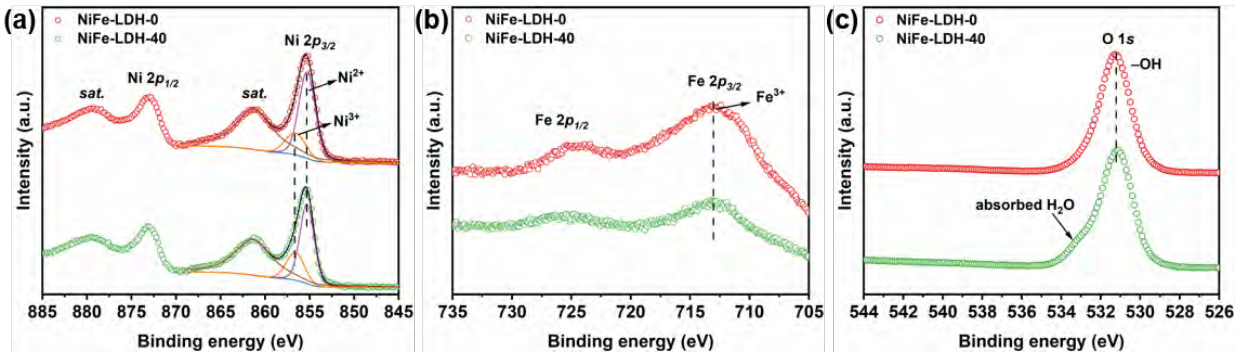

Fig. S10. XPS spectra of NiFe-LDH-0 and NiFe-LDH-40: (a) Ni 2*p*, (b) Fe 2*p*, and (c) O 1*s*.

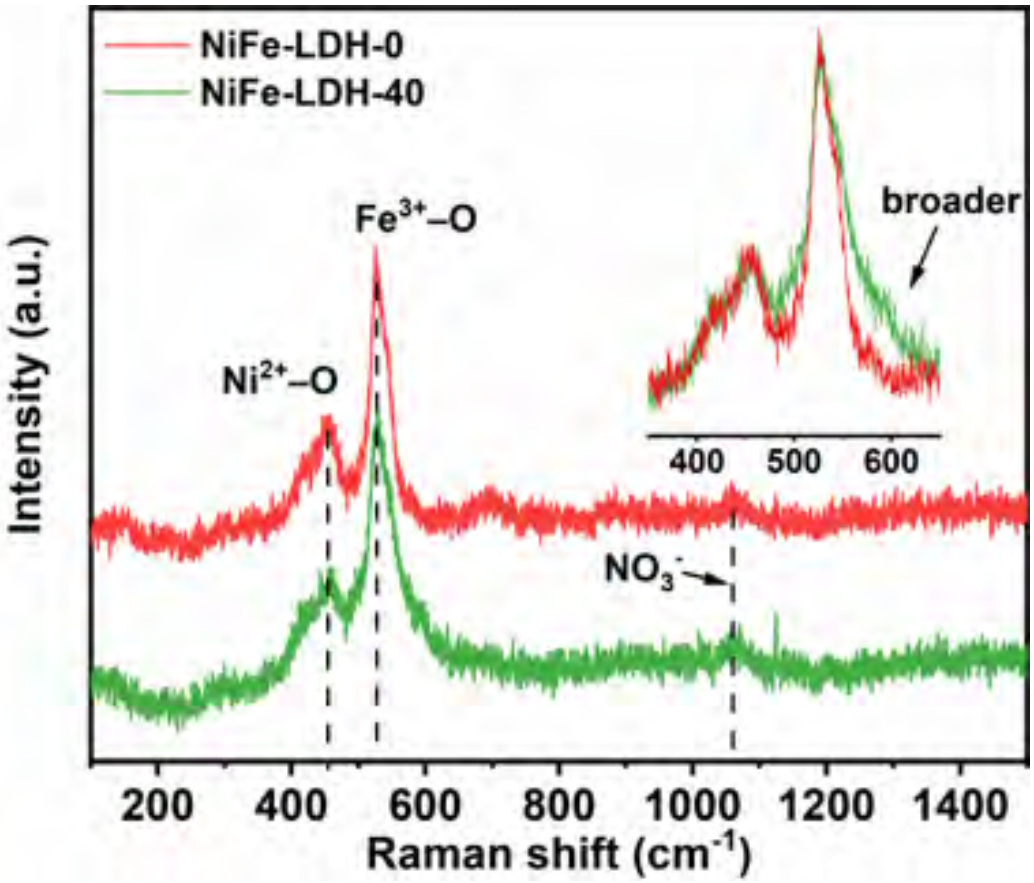

Fig. S11. Raman scattering spectra of dry NiFe-LDH-0 and NiFe-LDH-40.

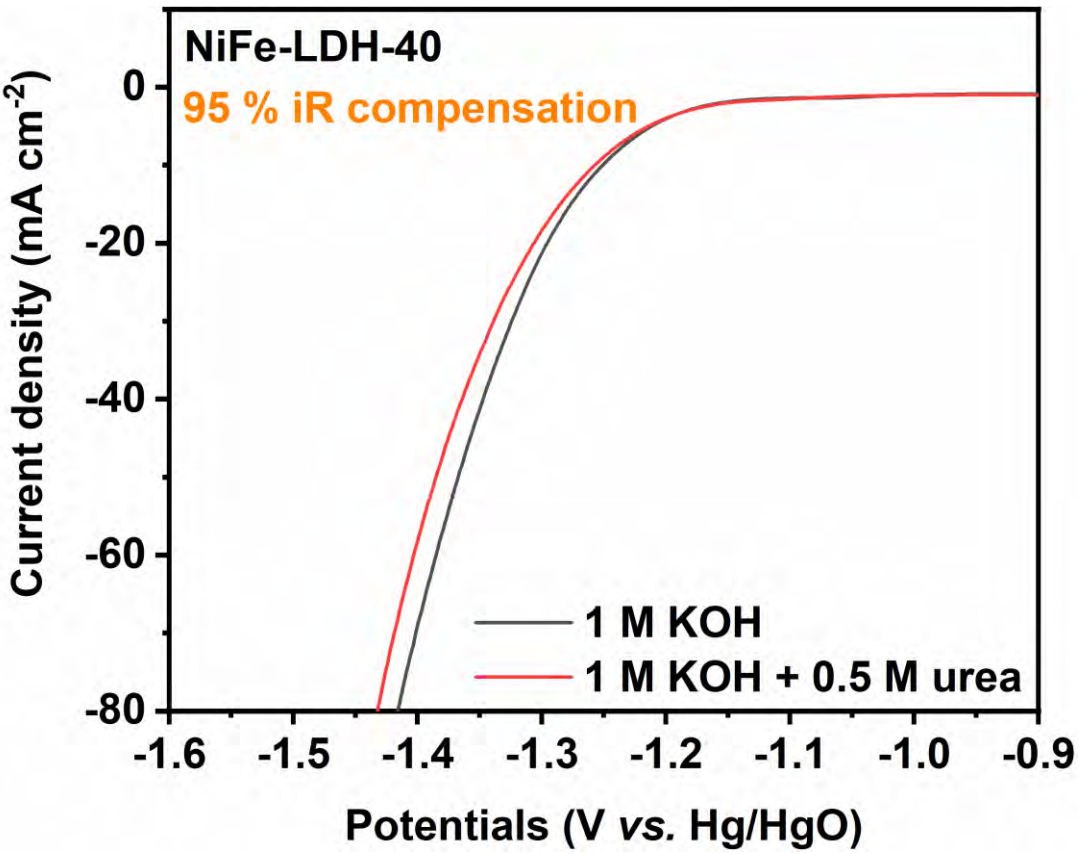

Fig. S12. Alkaline HER properties of NiFe-LDH-40 in urea-containing and urea-free electrolytes.

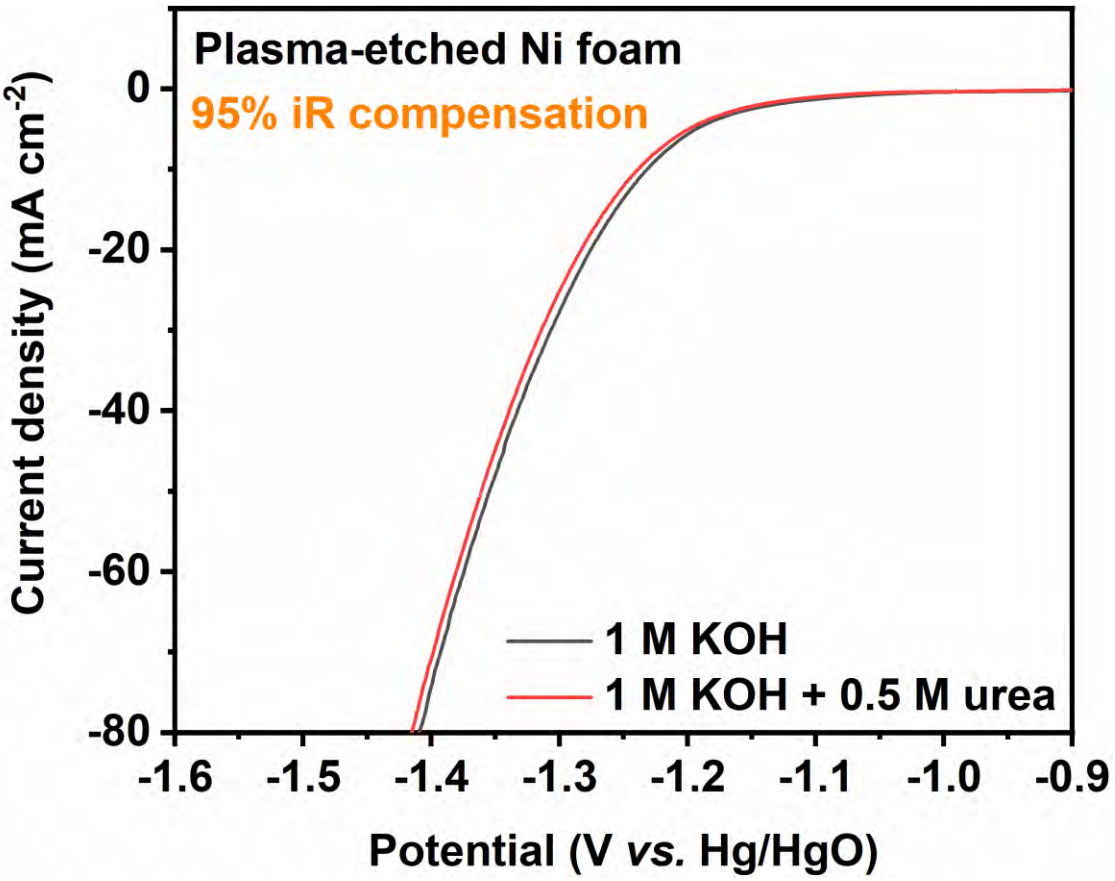

Fig. S13. Alkaline HER properties of the plasma-processed Ni foam in urea-containing and urea-free electrolytes.

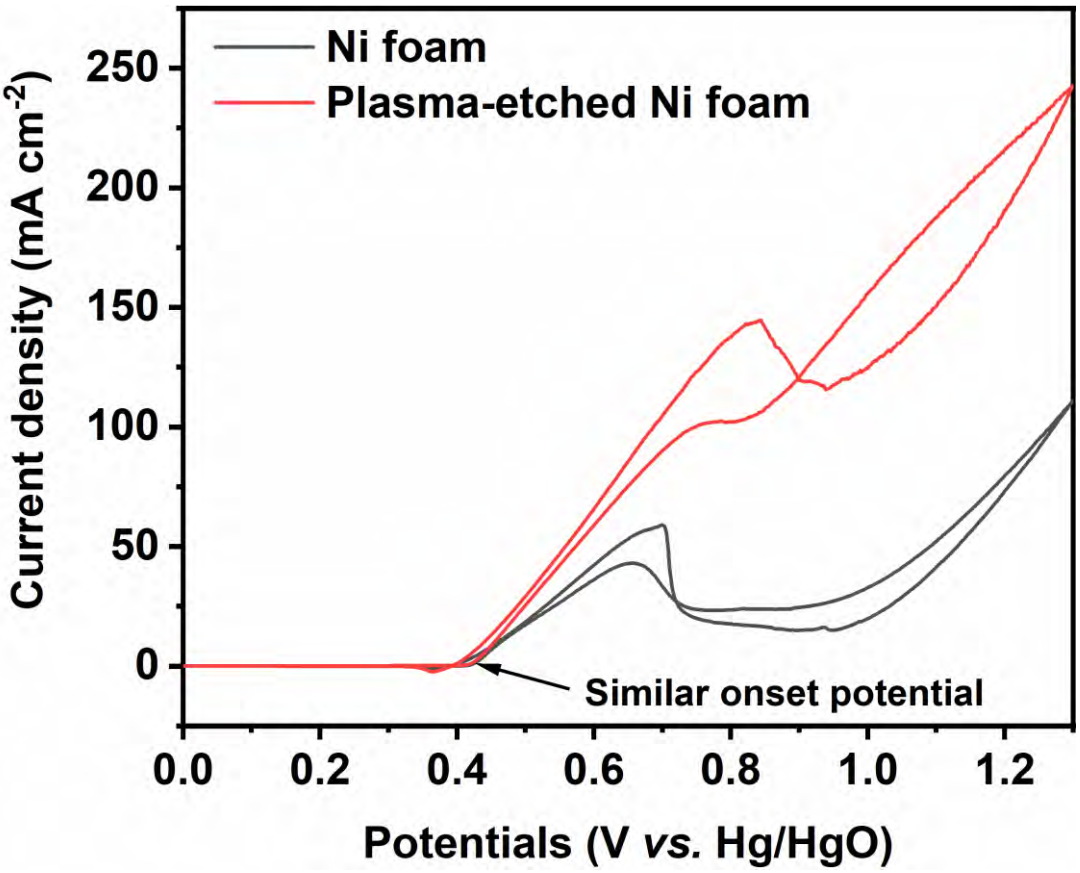

Fig. S14. UOR properties of the plasma-processed Ni foam and bare Ni foam.

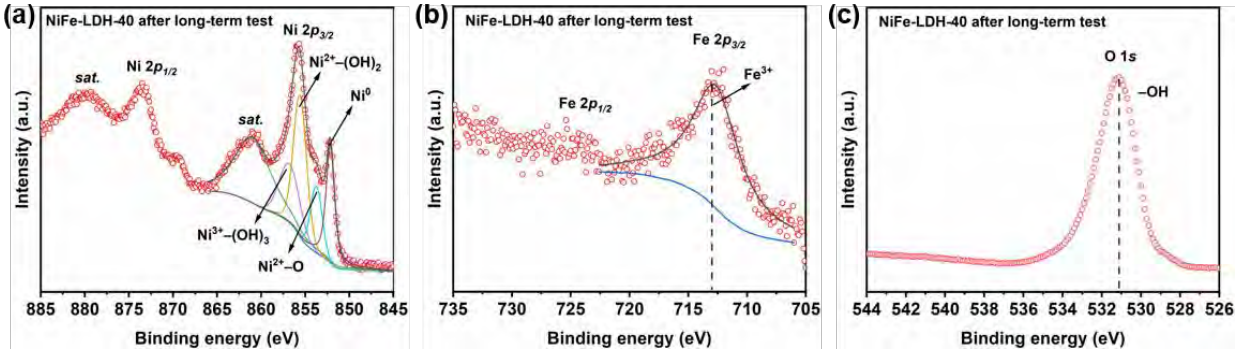

Fig. S15. XPS spectra of NiFe-LDH-40 after the 18-h stability test: (a) Ni 2*p*, (b) Fe 2*p*, and (c) O 1*s*. In the Ni 2*P* spectra, besides Ni^0 from the exposed Ni foam substrate, the new Ni^{2+}–O peak is related to unrecovered Ni(OH)5O- intermediates from dehydrogenation of $Ni(OH)_6$ octahedrons. The initial XPS spectra of NiFe-LDH-40 are shown in Figure S10.